

Gravitational waves from spinning black hole-neutron star binaries: dependence on black hole spins and on neutron star equations of state

Koutarou Kyutoku, Hirotada Okawa, Masaru Shibata
Yukawa Institute for Theoretical Physics, Kyoto University, Kyoto 606-8502, Japan

Keisuke Taniguchi
Graduate School of Arts and Sciences, University of Tokyo, Komaba, Meguro, Tokyo 153-8902, Japan
 (Dated: October 30, 2018)

We study the merger of black hole-neutron star binaries with a variety of black hole spins aligned or anti-aligned with the orbital angular momentum, and with the mass ratio in the range $M_{\text{BH}}/M_{\text{NS}} = 2\text{--}5$, where M_{BH} and M_{NS} are the mass of the black hole and neutron star, respectively. We model neutron-star matter by systematically parametrized piecewise polytropic equations of state. The initial condition is computed in the puncture framework adopting an isolated horizon framework to estimate the black hole spin and assuming an irrotational velocity field for the fluid inside the neutron star. Dynamical simulations are performed in full general relativity by an adaptive-mesh refinement code, SACRA. The treatment of hydrodynamic equations and estimation of the disk mass are improved. We find that the neutron star is tidally disrupted irrespective of the mass ratio when the black hole has a moderately large prograde spin, whereas only binaries with low mass ratios, $M_{\text{BH}}/M_{\text{NS}} \lesssim 3$, or small compactnesses of the neutron stars bring the tidal disruption when the black hole spin is zero or retrograde. The mass of the remnant disk is accordingly large as $\gtrsim 0.1M_{\odot}$, which is required by central engines of short gamma-ray bursts, if the black hole spin is prograde. Information of the tidal disruption is reflected in a clear relation between the compactness of the neutron star and an appropriately defined ‘‘cutoff frequency’’ in the gravitational-wave spectrum, above which the spectrum damps exponentially. We find that the tidal disruption of the neutron star and excitation of the quasinormal mode of the remnant black hole occur in a compatible manner in high mass-ratio binaries with the prograde black hole spin. The correlation between the compactness and the cutoff frequency still holds for such cases. It is also suggested by extrapolation that the merger of an extremely spinning black hole and an irrotational neutron star binary does not lead to the formation of an overspinning black hole.

PACS numbers: 04.25.D-, 04.30.-w, 04.40.Dg

I. INTRODUCTION

Coalescing binaries composed of a black hole (BH) and/or a neutron star (NS) are among the most promising sources of gravitational waves for ground-based laser-interferometric gravitational-wave detectors such as LIGO [1] and VIRGO [2]. Detections of gravitational waves will be accomplished in a decade to come by planned next-generation detectors such as advanced LIGO, advanced VIRGO, and LCGT [3]. Because gravitational waves are much more transparent to the absorption and scattering by the material than electromagnetic waves and even neutrinos are, gravitational-wave astronomy is expected to become a powerful and unique way to observe strongly gravitating phenomena in our Universe. Among such phenomena, the merger of a BH-NS binary plays an important role to investigate properties of the NS such as the radius and the equation of state (EOS) of a high-density nuclear matter [4–9]. An important constraint on the EOS is obtained from detection of a $1.97 \pm 0.04M_{\odot}$ NS, which is the most massive NS currently known [10], by recent pulsar-timing observation. However, we still do not know the realistic EOS of the NS because there is no robust measurement of the NS radius [11]. To constrain the NS radius and EOS by observing gravitational waves from the BH-NS binary, we

have to prepare accurate theoretical templates of gravitational waveforms employing a wide variety of the NS EOSs and other physical parameters. For this purpose, numerical relativity is the unique approach.

The merger of a BH-NS binary is also an important target for the astrophysical study because it is a potential candidate for the progenitor of short-hard gamma-ray bursts (GRBs) in the so-called merger scenario (see Refs. [12, 13] and references therein for reviews). If a NS is tidally disrupted during the merger of a BH-NS binary, a system composed of a spinning BH and a hot, massive accretion disk of $\gtrsim 0.01M_{\odot}$ may be formed. Such an outcome could be a central engine of the GRB, because it could radiate a large amount of energy $\gtrsim 10^{48}$ erg via neutrino emission or the Blandford-Znajek mechanism [14] in a short time scale of $\lesssim 2$ s and hence could launch a GRB jet. The merger scenario of the GRB is attractive when a short-hard GRB is associated with a galaxy of low star-formation rate [15, 16] because the collapsar model of GRBs [17] is not preferable. Only numerical relativity can answer quantitatively the question whether the formation of a massive accretion disk is possible in the BH-NS binary merger.

Fully general relativistic study of BH-NS binaries has achieved progress in recent years, both in computations of quasiequilibrium states [18–22] and in dynamical sim-

ulations of the merger [23–32]. Although these include several simulations of spinning BH-NS binaries with a qualitative $\Gamma = 2$ ideal-gas EOS, to date, only limited number of simulations have been performed taking into account both the nuclear-theory based EOS and the BH spin [30]. In particular, we still do not understand the dependence of the merger process and resulting gravitational waveforms on the BH spin and the EOS of the NS in detail. One goal of current numerical relativity is to clarify the effect of the BH spin on the BH-NS binary merger and subsequent NS tidal disruption adopting a wide variety of the NS EOSs.

In this paper, we report our latest results obtained by numerical-relativity simulations with a variety of the NS EOSs and the BH spins. We employ five piecewise polytropic EOSs (see Sec. II B), all of which do not conflict with the current observation of the $1.97 \pm 0.04 M_{\odot}$ NS. We systematically choose physical parameters such as BH mass, NS mass, and BH spin in an astrophysically realistic range. While we only consider relatively low mass BHs in the previous work [31], we adopt a wider range of the BH mass because a large BH spin enhances the NS tidal disruption for high mass-ratio binaries. We clarify the dependence on the BH spin and on the NS EOS of the properties of the merger remnants and characteristics of gravitational waves—in particular, the gravitational-wave spectrum.

This paper is organized as follows. In Sec. II, we describe methods for a solution of initial conditions, piecewise polytropic EOSs, and models of BH-NS binaries employed in this paper. In Sec. III, the formulation and methods of numerical simulations are summarized. Section IV presents the numerical results and clarifies the effect of the BH spin and NS EOS on the tidal disruption, merger remnants, and gravitational waves. Section V is devoted to a summary. Throughout this paper, we adopt the geometrical units in which $G = c = 1$, where G and c are the gravitational constant and the speed of light, respectively. Our convention of notation for physically important quantities is summarized in Table I. The nondimensional spin parameter of the BH, total mass of the system at infinite separation, mass ratio, and compactness of the NS are defined as $a = S_{\text{BH}}/M_{\text{BH}}^2$, $m_0 = M_{\text{BH}} + M_{\text{NS}}$, $Q = M_{\text{BH}}/M_{\text{NS}}$, and $\mathcal{C} = M_{\text{NS}}/R_{\text{NS}}$, respectively. Latin and Greek indices denote spatial and spacetime components, respectively.

II. INITIAL CONDITION

As in our previous works [29, 31], we employ BH-NS binaries in quasiequilibrium states for initial conditions of our numerical simulations. In this section, we summarize the formulation and methods for the computation of a quasiequilibrium state, specifically our method of estimating the spin angular momentum of the BH in a binary and of determining the position of the rotation axis. The details of the formulation and numerical meth-

TABLE I. Our convention of notation for physically important quantities.

Symbol	
M_{irr}	The irreducible mass of the BH
S_{BH}	The magnitude of the BH spin angular momentum
M_{BH}	The gravitational mass of the BH in isolation
M_{NS}	The gravitational mass of the NS in isolation
R_{NS}	The circumferential radius of the NS in isolation
M_0	The Arnowitt-Deser-Misner mass of the system
m_0	The total mass of the system at infinite separation
Q	The mass ratio
\mathcal{C}	The compactness of the NS
a	The nondimensional spin parameter of the BH

ods, except for the issues on the BH spin, are described in Ref. [22], to which the reader may refer. Computations of the quasiequilibrium states are performed using the spectral-method library LORENE [33].

A. Formulation and methods

We compute a quasiequilibrium state of the BH-NS binary as a solution of the initial value problem of general relativity [34]. As far as the orbital separation is large enough, the time scale of the orbital contraction due to the gravitational radiation reaction is much longer than the orbital period, and, therefore, we may safely neglect the gravitational radiation reaction in the calculation of the quasiequilibrium state. In numerical simulations of the binary coalescences, we have to track $\gtrsim 5$ orbits in order to calculate accurate gravitational waveforms during the late inspiral and merger phases, and hence, the orbital separation of the initial condition has to be large enough. For such initial conditions, we can neglect the gravitational radiation reaction. Thus, we give a BH-NS binary in a quasicircular orbit, i.e., the binary in an approximate equilibrium state in the corotating frame. To satisfy the quasiequilibrium requirements described above, we assume the existence of a helical Killing vector with the orbital angular velocity Ω ,

$$\xi^\mu = (\partial_t)^\mu + \Omega(\partial_\varphi)^\mu. \quad (1)$$

We also assume that the NS is in the hydrostatic equilibrium in the corotating frame and has an irrotational velocity field, which is believed to be a reliable approximation to an astrophysically realistic configuration [35, 36].

We compute the three-metric γ_{ij} , the extrinsic curvature K_{ij} , the lapse function α , and the shift vector β^i by a mixture of the extended conformal thin-sandwich approach [37, 38] and the conformal transverse-traceless decomposition [34] in the puncture framework [39–41]. In this formalism, we assume the conformal flatness of the three-metric $\gamma_{ij} = \psi^4 \hat{\gamma}_{ij} = \psi^4 f_{ij}$, the stationarity of the conformal three-metric $\mathcal{L}_\xi \hat{\gamma}_{ij} = 0$, the maximal slicing

condition $K = \gamma^{ij}K_{ij} = 0$, and its preservation in time $\mathcal{L}_\xi K = 0$, where f_{ij} is the flat spatial metric. Assuming that the puncture is located at x_{P}^i , we set the conformal factor ψ and a weighted lapse function $\Phi \equiv \alpha\psi$ as

$$\psi = 1 + \frac{M_{\text{P}}}{2r_{\text{BH}}} + \phi, \quad \Phi = 1 - \frac{M_{\Phi}}{2r_{\text{BH}}} + \eta, \quad (2)$$

where M_{P} and M_{Φ} are positive constants of mass dimension, and $r_{\text{BH}} = |x^i - x_{\text{P}}^i|$ is a coordinate distance from the puncture. We adjust M_{P} to obtain a desired mass of the BH, M_{BH} , and determine M_{Φ} so as to satisfy the virial relation, i.e., the equality of the Arnowitt-Deser-Misner (ADM) mass and the Komar mass, which holds when the spacetime is stationary and asymptotically flat [42, 43]. ϕ , β^i , and η are determined by solving elliptic equations derived from the Hamiltonian constraint, momentum constraint, and quasiequilibrium conditions, $\mathcal{L}_\xi \hat{\gamma}_{ij} = 0$ and $\mathcal{L}_\xi K = 0$. We note that these quasiequilibrium conditions can be replaced by $\partial_t \hat{\gamma}_{ij} = 0$ and $\partial_t K = 0$ in a conformal flatness approximation. In the puncture framework, we also decompose a conformally weighted extrinsic curvature $\hat{A}_{ij} = \psi^2 K_{ij}$ as

$$\hat{A}_{ij} = \hat{\nabla}_i W_j + \hat{\nabla}_j W_i - \frac{2}{3} f_{ij} \hat{\nabla}^k W_k + K_{ij}^{\text{P}}, \quad (3)$$

where W_i is an auxiliary three-vector field and $\hat{\nabla}_i$ is the covariant derivative associated with f_{ij} . K_{ij}^{P} is a singular part of the extrinsic curvature, which is associated with the linear and spin angular momenta of the BH [44],

$$K_{ij}^{\text{P}} = \frac{3}{2r_{\text{BH}}^2} [l_i P_j^{\text{BH}} + l_j P_i^{\text{BH}} - (f_{ij} - l_i l_j) l^k P_k^{\text{BH}}] + \frac{3}{r_{\text{BH}}^3} [\epsilon_{kil} S_{\text{P}}^l l_j + \epsilon_{kjl} S_{\text{P}}^l l_i], \quad (4)$$

where $l^i = x_{\text{BH}}^i / r_{\text{BH}}$ is a unit radial vector, $l_i = f_{ij} l^j$, and ϵ_{ijk} is the Levi-Civita tensor associated with the flat metric f_{ij} . P_i^{BH} and S_{P}^i are parameters associated with the linear and spin angular momenta of the BH, respectively. Here we determine P_i^{BH} by the condition in which the total linear momentum of the binary vanishes, and we adjust S_{P}^i to obtain a desired spin angular momentum of the BH, S_{BH}^i . The elliptic equation to determine W_i is obtained by taking the derivative of Eq. (3) and using the momentum constraint.

The spin angular momentum of the BH, S_{BH}^i , is evaluated on the apparent horizon (hereafter AH), \mathcal{S} , according to the isolated horizon framework (see Refs. [45, 46] for reviews). Because we do not know the position of the AH in advance in the puncture framework, we have to determine the location of the AH numerically [47]. On the numerically determined AH, an approximate rotational Killing vector may be defined using the method developed by Cook and Whiting [48] with the normalization condition proposed by Lovelace and his collaborators [49]. We focus only on the case in which the BH spin is aligned or antialigned with the angular momentum of the binary in this work, and hence, the axis of the BH spin

is uniquely determined. Hereafter we set the rotational axis of the binary, equivalently the axis of the BH spin, to be the z axis and consider only the approximate Killing vector ϕ^i associated with the rotation in this direction. Using ϕ^i , we obtain the spin angular momentum of the BH $S_{\text{BH}}^{(\phi)} = S_{\text{BH}}^z$ via the surface integral at the AH,

$$S_{\text{BH}}^{(\phi)} = \frac{1}{8\pi} \int_{\mathcal{S}} K_{ij} \phi^i dS^j. \quad (5)$$

We adjust S_{P}^z to obtain a desired value of S_{BH}^z (hereafter S_{BH}). We note that S_{P}^i and S_{BH}^i do not agree exactly in the BH-NS binary spacetime due to the contribution to the extrinsic curvature from the NS, associated with W_i .

Because we adopt a conformal flatness approximation for the induced metric, the Christodoulou mass of the BH evaluated on the AH, $M_{\mathcal{H}} = \sqrt{M_{\text{irr}}^2 + (S_{\text{BH}}^2/4M_{\text{irr}}^2)}$, and the gravitational mass evaluated at spatial infinity, M_{BH} , do not agree even for a single BH system due to the presence of so-called junk waves. This difference leads to an ambiguity in defining the nondimensional spin parameter of the BH. Here, we define the nondimensional spin parameter of the BH with respect to the mass evaluated at spatial infinity, i.e.,

$$a \equiv \frac{S_{\text{BH}}}{M_{\text{BH}}^2}. \quad (6)$$

The reason for this is that the mass and nondimensional spin parameter of the BH evaluated at the AH quickly (in our simulations, within ~ 1 ms) relax to M_{BH} and a , defined at spatial infinity, respectively, as the BH absorbs the junk radiation in the vicinity of the BH [49, 50]. We note that these values show the damping oscillation before the relaxation in the same manner as the ‘‘scalar-curvature spin’’ of Ref. [49] shows, because our method of evaluating these values in the simulation is basically the same as the method to define the scalar-curvature spin in Ref. [49] (see Sec. III B).

To compute the equations of hydrostatic equilibrium for the NS matter, we assume an ideal fluid, for which the energy-momentum tensor is described by

$$T^{\mu\nu} = \rho h u^\mu u^\nu + P g^{\mu\nu}, \quad (7)$$

where ρ is the rest-mass density, P is the pressure, $h \equiv 1 + \varepsilon + (P/\rho)$ is the specific enthalpy, ε is the specific internal energy, and u^μ is the four-velocity of the fluid. Basic equations for the hydrostatics are derived from the condition of irrotation, or the vanishing of the vorticity two-form [51–54],

$$\omega_{\mu\nu} = \nabla_\mu (h u_\nu) - \nabla_\nu (h u_\mu) = 0, \quad (8)$$

and the conservation of the specific momentum of the fluid along the helical Killing vector field $\mathcal{L}_\xi (h u_\mu) = 0$. The specific enthalpy is determined from the first integral of the relativistic Euler equation (relativistic Bernoulli integral), and other thermodynamical quantities are subsequently obtained by using the EOS, which is described

in Sec. II B. The four-velocity of the fluid is calculated using the velocity potential Ψ , as $hu_i = \partial_i \Psi$ in the assumption of the irrotational velocity field. The elliptic equation for Ψ is derived from the equation of continuity, $\nabla_\mu(\rho u^\mu) = 0$.

We have no definite condition to determine the location of the center of mass of the binary in the puncture framework and we use this ambiguity to reduce an unphysical initial orbital eccentricity. We found in our previous work [22, 29] that orbits with a small eccentricity could be obtained using the “3PN-J method,” i.e., a phenomenological method to determine the location of the rotational axis in which the total angular momentum of the binary for a given value of Ωm_0 agrees with that calculated from the third post-Newtonian (3PN) approximation. In the present case in which the BH has a finite amount of spin angular momentum, we extend the previous 3PN-J method to include the contribution from the BH spin up to the 2.5PN order [55, 56]. Specifically, the location of the rotational axis is chosen from the condition that the orbital angular momentum of the binary agrees with a sum of nonspin terms given by Eq. (4) of Ref. [57] and of spin terms given by Eq. (7.10) of Ref. [56] for a given value of Ωm_0 . We show in Sec. IV A that this extended 3PN-J method again leads to the initial condition with a small eccentricity.

B. Piecewise polytropic equations of state

The matter inside the NS in the late inspiral phase is believed to be well-approximated by a zero-temperature nuclear matter because the cooling time scale of the NS in typical BH-NS binaries is shorter than the time scale of the gravitational radiation reaction [58]. Hence, we employ a cold EOS, for which the rest-mass density, ρ , determines all other thermodynamical quantities, for calculating the quasiequilibrium state of the BH-NS binary. To model nuclear-theory-based EOSs at high density with a small number of parameters, we employ a piecewise polytropic EOS. It is a phenomenologically parametrized EOS of the form

$$P(\rho) = \kappa_i \rho^{\Gamma_i} \quad \text{for } \rho_{i-1} \leq \rho < \rho_i \quad (1 \leq i \leq n), \quad (9)$$

where n is the number of the pieces used to parametrize an EOS, ρ_i is the rest-mass density at the boundary of two neighboring i th and $(i+1)$ th pieces, κ_i is the polytropic constant for the i th piece, and Γ_i is the adiabatic index for the i th piece. Here, $\rho_0 = 0$, $\rho_n \rightarrow \infty$, and other parameters ($\rho_i, \kappa_i, \Gamma_i$) are freely chosen. Requiring the continuity of the pressure at each ρ_i , $2n$ free parameters—say (κ_i, Γ_i) —determine the EOS completely. The specific internal energy, ε , and hence the specific enthalpy, h , are determined by the first law of thermodynamics and continuity of each variable at boundary densities, ρ_i .

It was shown that piecewise polytropic EOSs with four pieces approximately reproduce most properties of the

nuclear-theory-based EOSs at high density [59]. If we focus on low mass NSs with relatively low central density, the EOS at high density plays a minor role. Thus, we adopt a simplified piecewise polytropic EOS composed of two pieces, one of which models the crust EOS and the other of which the core EOS. This simplification is based on the fact that NSs in the observed binary NSs often have fairly small masses $\lesssim 1.4M_\odot$ [60] and the maximum rest-mass density in such NSs may not be so high that the EOS at high density plays only a minor role in determining their structure. Furthermore, the maximum rest-mass density inside the NS should only decrease during the evolution of the BH-NS binary due to tidal elongation of the NS by the companion BH.

Table II lists the EOSs which we employ in this study. Following Refs. [6, 31], we always fix the EOS for the crust region by the parameters below:

$$\Gamma_1 = 1.35692395, \quad (10)$$

$$\kappa_1/c^2 = 3.99873692 \times 10^{-8} \text{ (g/cm}^3\text{)}^{1-\Gamma_1}. \quad (11)$$

The EOS of the core region is determined by two parameters. One is the adiabatic index of the core EOS, Γ_2 . Whereas we find that properties of gravitational waves and the merger remnants depend on Γ_2 in our previous study [31], we always fix $\Gamma_2 = 3$ in this work to focus on clarifying the effect of the BH spin aside from the difference in the adiabatic index. The other parameter is chosen to be the pressure p at a fiducial density $\rho_{\text{fidu}} = 10^{14.7} \text{ g/cm}^3$ because p is closely related to the radius and deformability of the NS [61]. We vary the value of p systematically to investigate the effect of the stiffness of the EOS [62]. With the given values of Γ_2 and p , κ_2 and ρ_1 are determined as

$$\kappa_2 = p \rho_{\text{fidu}}^{-\Gamma_2}, \quad (12)$$

$$\rho_1 = (\kappa_1/\kappa_2)^{1/(\Gamma_2-\Gamma_1)}. \quad (13)$$

C. Models

Numerical simulations are performed for a wide range of nondimensional BH spin parameter, a , as well as for a variety of the mass ratios, Q . For nonspinning BH-NS binaries, we already found that the low mass ratio of $Q \lesssim 3$ is required for tidal disruption of NSs to occur sufficiently outside the innermost stable circular orbit (ISCO) of the BH unless the EOS is extremely stiff [31]. If the tidal disruption occurs inside or at an orbit very close to the ISCO, we do not see strong effects of the tidal disruption. In such cases, gravitational waveforms are similar to those of a BH-BH binary even in the merger phase, and the mass of the remnant disk is negligible [63]. However, the allowed range of the mass ratio for the tidal disruption is modified drastically for a BH-NS binary with the prograde BH spin [64, 65] because the ISCO radius [66] of the BH with a prograde spin becomes smaller by a factor of 1–6 [67] than that of the nonspinning BH with

TABLE II. Key ingredients of the adopted EOSs. $\Gamma_2 (= 3.0)$ is the adiabatic index in the core region and p is the pressure at the fiducial density $\rho_{\text{fidu}} = 10^{14.7} \text{ g/cm}^3$, which determines the polytropic constant κ_2 of the core region and ρ_1 , the critical rest-mass density separating the crust and core regions. M_{max} is the maximum mass of the spherical NS for a given EOS. R_{135} (R_{12} , R_{145}) and \mathcal{C}_{135} (\mathcal{C}_{12} , \mathcal{C}_{145}) are the circumferential radius and the compactness of the NS with $M_{\text{NS}} = 1.35M_{\odot}$ ($1.2M_{\odot}$, $1.45M_{\odot}$).

Model	Γ_2	$\log_{10} p \text{ (g/cm}^3\text{)}$	$\rho_1 (10^{14} \text{ g/cm}^3)$	$M_{\text{max}} [M_{\odot}]$	$R_{135} \text{ (km)}$	\mathcal{C}_{135}	$R_{12} \text{ (km)}$	\mathcal{C}_{12}	$R_{145} \text{ (km)}$	\mathcal{C}_{145}
2H	3.0	13.95	0.7033	2.835	15.23	0.1309	15.12	0.1172	15.28	0.1401
1.5H	3.0	13.75	0.9308	2.525	13.69	0.1456	13.63	0.1300	13.72	0.1561
H	3.0	13.55	1.232	2.249	12.27	0.1624	12.25	0.1447	12.27	0.1744
HB	3.0	13.45	1.417	2.122	11.61	0.1718	11.60	0.1527	11.59	0.1848
B	3.0	13.35	1.630	2.003	10.96	0.1819	10.98	0.1614	10.93	0.1960

the same mass. Strong spin effects for the tidal disruption are also found in the numerical-relativity simulation of the spinning BH-NS binary merger with a simplified, Γ -law EOS [28]. In this paper we perform a more systematic study of the tidal disruption for different EOSs, masses of each component, and BH spins.

Table III summarizes several key quantities for the initial conditions in our numerical simulations. The label for the model denotes the EOS name, the mass ratio, the NS mass, and the nondimensional spin parameter of the BH. Specifically, “a75,” “a5,” and “a-5” correspond to the spin parameters $a = 0.75$, 0.5 , and -0.5 , respectively. For example, HB-Q3M135a5 means that the EOS is HB and $(Q, M_{\text{NS}}, a) = (3, 1.35M_{\odot}, 0.5)$. Although we vary the NS mass systematically, the results of the merger remnant are reported only for binaries with $M_{\text{NS}} = 1.35M_{\odot}$ in this paper because the difference in the NS mass complicates the properties of the remnant, such as the mass of the disk. Results for $M_{\text{NS}} \neq 1.35M_{\odot}$ are analyzed only for gravitational waves.

For the same value of the mass ratio, we basically prepare the initial conditions with the same value of the initial angular velocity Ω_0 normalized by the total mass of the binary, $\Omega_0 m_0$. For 2H EOS, in which the NS radius is the largest, we exceptionally adopt a smaller value of $\Omega_0 m_0$ than for other EOSs to guarantee $\gtrsim 5$ orbits before tidal disruption occurs. The reason for this is that the tidal disruption occurs for a large orbital separation in 2H EOS. When the BH has a prograde spin, the number of orbits to the merger for a given value of $\Omega_0 m_0$ increases due to spin-orbit repulsive interaction [68], compared to the nonspinning BH case. On the other hand, when the BH has a retrograde spin, the number of orbits decreases due to spin-orbit attractive interaction. For $a = -0.5$, the number of orbits is typically by ~ 1 orbit smaller than for $a = 0$. For this reason, we also prepare the initial condition with a smaller value of $\Omega_0 m_0$ for H EOS and $a = -0.5$.

III. METHODS OF SIMULATIONS

Numerical simulations are performed using an adaptive-mesh refinement (AMR) code SACRA [69]. The formulation, the gauge conditions, the numerical scheme,

and the methods of diagnostics are basically the same as those described in Ref. [31], except for the correction in the treatment of hydrodynamic equations in a far region. Thus, we here only briefly review them and describe the present setup of the computational domain for the AMR algorithm and grid resolution.

A. Formulation and numerical methods

SACRA solves the Einstein evolution equations in the Baumgarte-Shapiro-Shibata-Nakamura (BSSN) formalism [70, 71] with the moving-puncture gauge [39–41]. It evolves a conformal factor $W \equiv \gamma^{-1/6}$, the conformal metric $\tilde{\gamma}_{ij} \equiv \gamma^{-1/3} \gamma_{ij}$, the trace of the extrinsic curvature K , a conformally weighted trace-free part of the extrinsic curvature $\tilde{A}_{ij} \equiv \gamma^{-1/3} (K_{ij} - K \gamma_{ij})$, and an auxiliary variable $\tilde{\Gamma}^i \equiv -\partial_j \tilde{\gamma}^{ij}$. Introducing an auxiliary variable B^i and a parameter η_s , which we typically set to be $\sim M_{\text{BH}}/M_{\odot}$ in units of $c = G = M_{\odot} = 1$, we employ a moving-puncture gauge in the form [72]

$$(\partial_t - \beta^j \partial_j) \alpha = -2\alpha K, \quad (14)$$

$$(\partial_t - \beta^j \partial_j) \beta^i = (3/4) B^i, \quad (15)$$

$$(\partial_t - \beta^j \partial_j) B^i = (\partial_t - \beta^j \partial_j) \tilde{\Gamma}^i - \eta_s B^i. \quad (16)$$

We evaluate the spatial derivative by a fourth-order central finite difference, except for the advection terms, which are evaluated by a fourth-order noncentered, upwind finite difference, and employ a fourth-order Runge-Kutta method for the time evolution.

To solve the hydrodynamic equations, we evolve $\rho_* \equiv \rho \alpha u^t W^{-3}$, $\hat{u}_i \equiv h u_i$, and $e_* \equiv h \alpha u^t - P/(\rho \alpha u^t)$. The advection terms are handled with a high-resolution central scheme by Kurganov and Tadmor [73] with a third-order piecewise parabolic interpolation for the cell reconstruction. For the EOS, we decompose the pressure and specific internal energy into cold and thermal parts as

$$P = P_{\text{cold}} + P_{\text{th}}, \quad \varepsilon = \varepsilon_{\text{cold}} + \varepsilon_{\text{th}}. \quad (17)$$

We calculate the cold parts of both variables using the piecewise polytropic EOS from the primitive variable ρ , and then the thermal part of the specific internal energy is defined from ε as $\varepsilon_{\text{th}} = \varepsilon - \varepsilon_{\text{cold}}$. Because ε_{th} vanishes

TABLE III. Key parameters and quantities for the initial conditions adopted in numerical simulations. The adopted EOS, mass ratio (Q), NS mass in isolation (M_{NS}), nondimensional spin parameter of the BH (a), initial angular velocity (Ω_0) in units of c^3/Gm_0 , baryon rest mass (M_*), compactness of the NS in isolation (\mathcal{C}), maximum rest-mass density (ρ_{max}), ADM mass of the system (M_0), and total angular momentum of the system (J_0), respectively. See also [31] for models of nonspinning BH-NS binaries.

Model	EOS	Q	$M_{\text{NS}}[M_{\odot}]$	a	$G\Omega_0 m_0/c^3$	$M_*[M_{\odot}]$	\mathcal{C}	$\rho_{\text{max}}(10^{14}\text{g/cm}^3)$	$M_0[M_{\odot}]$	$J_0[GM_{\odot}^2/c]$
2H-Q2M135a75	2H	2	1.35	0.75	0.025	1.455	0.1309	3.740	4.014	13.83
1.5H-Q2M135a75	1.5H	2	1.35	0.75	0.028	1.468	0.1456	5.104	4.012	13.42
H-Q2M135a75	H	2	1.35	0.75	0.028	1.484	0.1624	7.019	4.012	13.42
HB-Q2M135a75	HB	2	1.35	0.75	0.028	1.493	0.1718	8.263	4.012	13.42
B-Q2M135a75	B	2	1.35	0.75	0.028	1.503	0.1819	9.762	4.012	13.42
2H-Q2M135a5	2H	2	1.35	0.5	0.025	1.455	0.1309	3.740	4.014	14.02
1.5H-Q2M135a5	1.5H	2	1.35	0.5	0.028	1.468	0.1456	5.104	4.012	13.63
H-Q2M135a5	H	2	1.35	0.5	0.028	1.484	0.1624	7.018	4.012	13.63
HB-Q2M135a5	HB	2	1.35	0.5	0.028	1.493	0.1718	8.263	4.012	13.63
B-Q2M135a5	B	2	1.35	0.5	0.028	1.503	0.1819	9.762	4.012	13.63
2H-Q2M135a-5	2H	2	1.35	-0.5	0.022	1.455	0.1309	3.740	4.019	15.15
H-Q2M135a-5	H	2	1.35	-0.5	0.025	1.484	0.1624	7.018	4.017	14.74
HB-Q2M135a-5	HB	2	1.35	-0.5	0.028	1.493	0.1718	8.262	4.015	14.41
B-Q2M135a-5	B	2	1.35	-0.5	0.028	1.503	0.1819	9.760	4.015	14.41
2H-Q2M12a75	2H	2	1.2	0.75	0.025	1.282	0.1172	3.465	3.568	10.93
H-Q2M12a75	H	2	1.2	0.75	0.028	1.303	0.1447	6.421	3.566	10.60
HB-Q2M12a75	HB	2	1.2	0.75	0.028	1.310	0.1527	7.523	3.566	10.60
B-Q2M12a75	B	2	1.2	0.75	0.028	1.317	0.1614	8.833	3.566	10.60
2H-Q2M145a75	2H	2	1.45	0.75	0.025	1.572	0.1401	3.926	4.312	15.96
H-Q2M145a75	H	2	1.45	0.75	0.028	1.607	0.1744	7.452	4.309	15.48
HB-Q2M145a75	HB	2	1.45	0.75	0.028	1.617	0.1848	8.811	4.309	15.48
B-Q2M145a75	B	2	1.45	0.75	0.028	1.629	0.1960	10.46	4.309	15.48
2H-Q3M135a75	2H	3	1.35	0.75	0.028	1.455	0.1309	3.737	5.357	20.00
1.5H-Q3M135a75	1.5H	3	1.35	0.75	0.030	1.468	0.1456	5.100	5.355	19.64
H-Q3M135a75	H	3	1.35	0.75	0.030	1.484	0.1624	7.013	5.355	19.64
HB-Q3M135a75	HB	3	1.35	0.75	0.030	1.493	0.1718	8.256	5.355	19.64
B-Q3M135a75	B	3	1.35	0.75	0.030	1.503	0.1819	9.753	5.355	19.63
2H-Q3M135a5	2H	3	1.35	0.5	0.028	1.455	0.1309	3.737	5.357	20.36
1.5H-Q3M135a5	1.5H	3	1.35	0.5	0.030	1.468	0.1456	5.100	5.356	20.02
H-Q3M135a5	H	3	1.35	0.5	0.030	1.484	0.1624	7.012	5.356	20.01
HB-Q3M135a5	HB	3	1.35	0.5	0.030	1.493	0.1718	8.255	5.356	20.01
B-Q3M135a5	B	3	1.35	0.5	0.030	1.503	0.1819	9.753	5.356	20.01
HB-Q3M135a-5	HB	3	1.35	-0.5	0.030	1.493	0.1718	8.253	5.359	21.46
2H-Q3M145a75	2H	3	1.45	0.75	0.028	1.572	0.1401	3.923	5.754	23.07
H-Q3M145a75	H	3	1.45	0.75	0.030	1.607	0.1744	7.445	5.751	22.65
HB-Q3M145a75	HB	3	1.45	0.75	0.030	1.617	0.1848	8.803	5.751	22.65
B-Q3M145a75	B	3	1.45	0.75	0.030	1.629	0.1960	10.45	5.751	22.65
2H-Q4M135a75	2H	4	1.35	0.75	0.030	1.455	0.1309	3.735	6.702	26.07
H-Q4M135a75	H	4	1.35	0.75	0.032	1.484	0.1624	7.007	6.700	25.62
HB-Q4M135a75	HB	4	1.35	0.75	0.032	1.493	0.1718	8.249	6.700	25.63
B-Q4M135a75	B	4	1.35	0.75	0.032	1.503	0.1819	9.746	6.700	25.62
2H-Q4M135a5	2H	4	1.35	0.5	0.035	1.455	0.1309	3.732	6.698	25.64
H-Q4M135a5	H	4	1.35	0.5	0.035	1.484	0.1624	7.004	6.698	25.63
HB-Q4M135a5	HB	4	1.35	0.5	0.035	1.493	0.1718	8.244	6.698	25.63
B-Q4M135a5	B	4	1.35	0.5	0.035	1.503	0.1819	9.740	6.698	25.63
2H-Q5M135a75	2H	5	1.35	0.75	0.036	1.455	0.1309	3.730	8.044	30.95
H-Q5M135a75	H	5	1.35	0.75	0.036	1.484	0.1624	7.000	8.044	30.95
HB-Q5M135a75	HB	5	1.35	0.75	0.036	1.493	0.1718	8.241	8.044	30.95
B-Q5M135a75	B	5	1.35	0.75	0.036	1.503	0.1819	9.736	8.043	30.95

in the absence of shock heating, ε_{th} is regarded as the finite-temperature part. In this paper, we adopt a Γ -law ideal-gas EOS for the thermal part,

$$P_{\text{th}} = (\Gamma_{\text{th}} - 1)\rho\varepsilon_{\text{th}}, \quad (18)$$

to determine the thermal part of the pressure, and choose Γ_{th} equal to the adiabatic index in the crust region, Γ_1 , for simplicity.

Because the vacuum is not allowed in any conservative hydrodynamic scheme, we put an artificial atmosphere of a small density outside the NS in the same way as done in our previous work [31]. The total rest mass of the atmosphere is always less than $10^{-4}M_{\odot}$, and hence, we can safely neglect spurious effects by accretion of the atmosphere onto the remnant disk as long as the disk mass is much larger than $10^{-4}M_{\odot}$.

B. Diagnostics

We extract gravitational waves by calculating the outgoing part of the Weyl scalar Ψ_4 at finite coordinate radii $r = 400\text{--}800M_{\odot}$ and by integrating Ψ_4 twice in time as

$$h_+(t) - ih_{\times}(t) = - \int^t dt' \int^{t'} dt'' \Psi_4(t''). \quad (19)$$

In our previous works [29, 31], we directly perform this integration of $\Psi_4(t)$ and then subtract a quadratic function of the form $a_2t^2 + a_1t + a_0$ to eliminate unphysical drift components in the waveform, using the least-square fitting to obtain constants a_0 , a_1 , and a_2 . In this work, we adopt a ‘‘fixed-frequency integration’’ method

proposed by Reisswig and Pollney [74] to obtain gravitational waveforms with less unphysical components. In this method, we first perform a Fourier transformation of Ψ_4 as

$$\tilde{\Psi}_4(\omega) = \int dt \Psi_4(t) e^{i\omega t}. \quad (20)$$

Using this, Eq. (19) is rewritten as

$$h_+(t) - ih_{\times}(t) = \frac{1}{2\pi} \int \frac{\tilde{\Psi}_4(\omega)}{\omega^2} e^{-i\omega t} d\omega. \quad (21)$$

We then replace $1/\omega^2$ of the integrand with $1/\omega_0^2$ for $|\omega| < \omega_0$, where ω_0 is a positive free parameter in this method. By appropriately choosing ω_0 , this procedure suppresses unphysical, low-frequency components of gravitational waves. As proposed in Ref. [74], we choose ω_0 to be $\sim 0.8m\Omega_0$ for $m \neq 0$ mode gravitational waves, where m is the azimuthal quantum number. For the $m = 0$ mode gravitational waves, we adopt $\omega_0 \sim 0.8\Omega_0$ and confirm that our results depend only very weakly on this choice. We also adopt this method to calculate the energy ΔE and angular momentum ΔJ radiated by gravitational waves. Exceptionally, we adopt the previous method of direct time integration to estimate the orbital eccentricity in the inspiral phase because the fixed-frequency integration method may change the modulation in the gravitational waveform.

For comparisons between numerically calculated gravitational waveforms and those calculated in the PN approximations, we use the Taylor-T4 formula for two-point masses in circular orbits [75] with an additional contribution from the BH spin angular momentum [76]. In this formula, the time evolution of the orbital angular velocity $\Omega(t)$ and orbital phase $\Theta(t)$ are computed using a nondimensional angular velocity $X(t) \equiv [m_0\Omega(t)]^{2/3}$ by

$$\begin{aligned} \frac{dX}{dt} = & \frac{64\nu X^5}{5m_0} \left[1 - \left(\frac{743}{336} + \frac{11}{4}\nu \right) X + \left(4\pi - \frac{113}{12}\chi + \frac{19}{6}\nu a \right) X^{3/2} \right. \\ & + \left(\frac{34103}{18144} + 5\chi^2 + \frac{13661}{2016}\nu + \frac{59}{18}\nu^2 \right) X^2 \\ & - \left\{ \left(\frac{4159}{672} + \frac{189}{8}\nu \right) \pi + \left(\frac{31571}{1008} - \frac{1165}{24}\nu \right) \chi + \frac{3}{4}\chi^3 - \left(\frac{21863}{1008}\nu - \frac{79}{6}\nu^2 \right) a \right\} X^{5/2} \\ & + \left\{ \frac{16447322263}{139708800} - \frac{1712}{105}\gamma_E + \frac{16}{3}\pi^2 - \left(\frac{56198689}{217728} - \frac{451}{48}\pi^2 \right) \nu + \frac{541}{896}\nu^2 - \frac{5605}{2592}\nu^3 \right. \\ & - \frac{856}{105} \ln(16X) - \frac{80\pi}{3}\chi + \left(\frac{64153}{1008} - \frac{457}{36}\nu \right) \chi^2 + \left(\frac{20}{3}\pi - \frac{1135}{36}\chi \right) \nu a \left. \right\} X^3 \\ & - \left\{ \left(\frac{4415}{4032} - \frac{358675}{6048}\nu - \frac{91495}{1512}\nu^2 \right) \pi + \left(\frac{2529407}{27216} - \frac{845827}{6048}\nu + \frac{41551}{864}\nu^2 \right) \chi - 12\pi\chi^2 \right. \\ & \left. + \left(\frac{1505}{24} + \frac{\nu}{8} \right) \chi^3 - \left(\frac{1580239}{54432} - \frac{451597}{6048}\nu^2 + \frac{2045}{432}\nu^3 + \frac{107}{6}\nu\chi^2 \right) a \right\} X^{7/2} \right], \quad (22) \end{aligned}$$

$$\frac{d\Theta}{dt} = \frac{X^{3/2}}{m_0}, \quad (23)$$

where $\nu \equiv Q/(1+Q)^2$, $\chi = aQ/(1+Q)$, and $\gamma_E \approx 0.5772$

is the Euler constant. After $X(t)$ and $\Theta(t)$ are obtained, we calculate the complex gravitational-wave amplitude

$$\begin{aligned}
h^{22} = & -8\sqrt{\frac{\pi}{5}}\frac{\nu m_0}{D}e^{-2i\Theta}X\left[1 - \left(\frac{107}{42} - \frac{55}{42}\nu\right)X + \left(2\pi - \frac{4}{3}\chi + \frac{2}{3}\nu a\right)X^{3/2}\right. \\
& - \left(\frac{2173}{1512} + \frac{1069}{216}\nu - \frac{2047}{1512}\nu^2\right)X^2 - \left\{\left(\frac{107}{21} - \frac{34}{21}\nu\right)\pi + 24i\nu\right\}X^{5/2} \\
& + \left\{\frac{27027409}{646800} - \frac{856}{105}\gamma_E + \frac{2}{3}\pi^2 - \frac{428}{105}\ln(16X) - \left(\frac{278185}{33264} - \frac{41}{96}\pi^2\right)\nu - \frac{20261}{2772}\nu^2\right. \\
& \left. + \frac{114635}{99792}\nu^3 + \frac{428}{105}i\pi\right\}X^3], \tag{24}
\end{aligned}$$

where D is the distance between the center of mass of the binary and an observer. Hereafter, we simply refer to this formula as the Taylor-T4 formula irrespective of the presence of the BH spin. Another way for deriving an approximate waveform is to employ an effective one-body approach (see Ref. [78] and references therein for reviews). In accompanied papers [63], comparisons between numerical waveforms and those of the effective one body approach are extensively performed.

To estimate the mass of the remnant disk, we calculate the total rest mass outside the AH

$$M_{r>r_{\text{AH}}} \equiv \int_{r>r_{\text{AH}}} \rho_* d^3x, \tag{25}$$

where $r_{\text{AH}} = r_{\text{AH}}(\theta, \varphi)$ is the radius of the AH as a function of the angular coordinates. We note that we systematically *underestimated* disk masses in our previous works performed with an old version of SACRA [29, 31], because we evolved hydrodynamic variables and estimated disk masses only in the finer domains (described in Sec. III C) of the size $\sim 200^3 \text{ km}^3$. Such a domain size is insufficient for the estimation of the disk mass if tidal disruption occurs at a distant orbit, especially for the case in which the NS radius is large ($\sim 15 \text{ km}$). In this study, we correct the treatment of hydrodynamics and the estimation of disk masses: We follow the hydrodynamics for a wide computational domain of the size $1000^3\text{--}2000^3 \text{ km}^3$. We still possibly underestimated disk masses because some of the material escapes from our computational domains and we cannot follow their return which would occur if they are bounded.

We determine key quantities of the remnant BH, i.e., the mass $M_{\text{BH},f}$ and nondimensional spin parameter a_f , from the circumferential radius of the AH, assuming that the deviation from the Kerr spacetime is negligible in the vicinity of a BH horizon. We estimate the remnant BH mass, $M_{\text{BH},f}$, from the circumferential radius of the AH along the equatorial plane C_e divided by 4π , i.e., $C_e/4\pi$, which gives the BH mass in the stationary vacuum BH spacetime. Similarly, the nondimensional spin parameter

h^{22} of the $(l, m) = (2, 2)$ mode and the spectrum up to the 3PN order using the formula shown in Refs. [76, 77]. Here, h^{22} is

of the remnant BH, a_f , is estimated from the ratio of the circumferential radius of the AH along the meridional plane C_p to C_e using the relation

$$\frac{C_p}{C_e} = \frac{\sqrt{2\hat{r}_+}}{\pi} E\left(\frac{a_f^2}{2\hat{r}_+}\right). \tag{26}$$

This also holds for the stationary vacuum BH with the nondimensional spin parameter a_f . Here, $\hat{r}_+ = 1 + \sqrt{1 - a_f^2}$ is a normalized radius of the horizon, and $E(z)$ is an elliptic integral

$$E(z) = \int_0^{\pi/2} \sqrt{1 - z \sin^2 \theta} d\theta. \tag{27}$$

For comparison, the nondimensional spin parameter of the remnant BH is also estimated from C_e and the irreducible mass of the remnant BH $M_{\text{irr},f}$ using the relation

$$M_{\text{irr},f} = \frac{C_e}{4\sqrt{2}\pi} \sqrt{1 + \sqrt{1 - a_f^2}}, \tag{28}$$

which holds for the stationary vacuum BH. The spin parameter obtained using this relation is referred to as a_{f2} according to Ref. [29]. Finally, we also estimate a_f from the values of the remnant BH computed using approximate conservation laws

$$M_{\text{BH},c} \equiv M_0 - M_{r>r_{\text{AH}}} - \Delta E, \tag{29}$$

$$J_{\text{BH},c} \equiv J_0 - J_{r>r_{\text{AH}}} - \Delta J, \tag{30}$$

where the total angular momentum of the material located outside the AH, $J_{r>r_{\text{AH}}}$, is approximately defined by

$$J_{r>r_{\text{AH}}} \equiv \int_{r>r_{\text{AH}}} \rho_* h u_\varphi d^3x. \tag{31}$$

Here, we assume that the orbital angular momentum of the BH is negligible. The nondimensional spin parameter of the remnant BH is defined by $a_{f1} \equiv J_{\text{BH},c}/M_{\text{BH},c}^2$, again according to Ref. [29].

C. Setup of AMR grids

In SACRA, an AMR algorithm is implemented so that both the radii of compact objects in the near zone and the characteristic gravitational wavelengths in the wave zone can be covered with sufficient grid resolutions simultaneously. Our AMR grids consist of a number of computational domains, each of which has the uniform, vertex-centered Cartesian grids with $(2N + 1, 2N + 1, N + 1)$ grid points for (x, y, z) with the equatorial plane symmetry at $z = 0$. We always choose $N = 50$ for the best resolved runs in this work. We also perform simulations with $N = 36$ and 42 for several arbitrary chosen models to check the convergence of the results and find approximately the same level of convergence as that found in the previous work (see the Appendix of Ref. [31]). In the Appendix of this paper, we show the convergence of gravitational waveforms and the masses of the remnant disks. The AMR grids are classified into two categories: one is a coarser domain, which covers a wide region, including both the BH and NS, with its origin fixed at the approximate center of mass throughout the simulation. The other is a finer domain, two sets of which comove with compact objects and cover the region in the vicinity of these objects. We denote the edge length of the largest domain, the number of the coarser domains, and the number of the finer domains by $2L$, l_c , and $2l_f$, respectively. Namely, the total number of the domains is $l_c + 2l_f$. The grid spacing for each domain is $h_l = L/(2^l N)$, where $l = 0 - (l_c + l_f - 1)$ is the depth of each domain.

Table IV summarizes the parameters of the grid structure for our simulations. The structure of the AMR grids depends primarily on the mass ratio of the binary because the distances between two objects and the center of mass depend strongly on the mass ratio for our initial models. Specifically, we choose $(l_c, l_f) = (4, 4)$ for all binaries with $M_{\text{NS}} = 1.35M_{\odot}$ and $Q = 2, 3$, and 4 . We choose $(l_c, l_f) = (3, 5)$ for binaries with $Q = 5$. For binaries with $M_{\text{NS}} \neq 1.35M_{\odot}$, we choose $(l_c, l_f) = (3, 4)$ because we do not evaluate disk masses for them. In all the simulations, L is chosen to be larger than or comparable to the gravitational wavelengths at an initial instant $\lambda_0 \equiv \pi/\Omega_0$. One of the two finest regions covers the semimajor axis of the NS by ~ 42 – 45 grid points. The other covers the coordinate radius of the AH typically by ~ 20 grid points, depending on the mass ratio and the BH spin. For the $Q = 5$ runs, the total memory required is about 11 G bytes. We perform numerical simulations with personal computers of 12 G bytes memory and of core-i7X processors with clock speeds of 3.2 or 3.33 GHz. We use 2–6 processors to perform one job with an OPEN-MP library. The typical computational time required to perform one simulation (for ~ 50 ms in physical time of coalescence for the $a = 0.75$ case) is 4 weeks for the 6 processor case.

IV. NUMERICAL RESULTS

We present numerical results of our simulations, focusing, in particular, on their dependence on the BH spin and NS EOS. First, we review general merger processes in Sec. IV A. Sections IV B, IV C, and IV D are devoted to the analysis of properties of the remnant disk and BH formed after the merger. Gravitational waveforms are shown in Sec. IV E, their spectra in Sec. IV F, and the energy and angular momentum radiated by gravitational waves in Sec. IV G.

A. Overview of the merger process

Figure 1 plots the evolution of the coordinate separation defined by $x_{\text{sep}}^i = x_{\text{NS}}^i - x_{\text{BH}}^i$ for models HB-Q2M135a5, HB-Q2M135, and HB-Q2M135a-5, for which $\Omega_0 m_0$ takes the same values. Here, x_{NS}^i is the position of the maximum rest-mass density and x_{BH}^i is the location of the puncture, x_{P}^i . Figure 1 shows that the numbers of orbits increases as the BH spin increases from retrograde to prograde [28]. Specifically, the number of orbit are $\sim 7, 5.5$, and 4 for $a = 0.5, 0$, and -0.5 , respectively. This difference comes primarily from the spin-orbit interaction between these two angular momenta [79]; in the PN approximation, a force proportional to the inner product of the orbital and spin angular momenta of two objects appears at 1.5PN order. Here, we do not have to consider the NS spin angular momentum in the assumption of the irrotational velocity field and, therefore, we only consider the interaction between the orbital and BH spin angular momenta throughout this paper. When these two angular momenta are parallel and the inner product is positive ($a > 0$), an additional repulsive force works between the BH and NS. This repulsive force reduces the orbital angular velocity because the centrifugal force associated with the orbital motion can be reduced, and hence, the luminosity of gravitational radiation, which is proportional to $\Omega^{10/3}$, is also reduced. This strong dependence of the luminosity on Ω makes the approaching velocity smaller in the late inspiral phase, and, therefore, the number of orbits increases. Conversely, when these two angular momenta are antiparallel ($a < 0$), an additional attractive force increases the angular velocity and gravitational-wave luminosity in the late inspiral phase. In this case, the orbital separation decreases faster due to a larger approaching velocity, and the number of orbits becomes smaller as the retrograde BH spin increases. All these results agree qualitatively with those of Ref. [28].

The fate of BH-NS binaries is classified into two categories. One is the case in which the NS is disrupted by the BH tidal field before the BH swallows the NS, and the other is the case in which the BH swallows the NS without tidal disruption. In this paper, we focus mainly on the former case. We plot snapshots of the rest-mass density profiles and the location of the AH on the equatorial

TABLE IV. Setup of the grid structure for the simulation with our AMR algorithm. l_c and l_f are the number of coarser domains and a half of finer domains, respectively. $\Delta x = h_l = L/(2^l N)$ ($l = l_c + l_f - 1$) is the grid spacing at the finest-resolution domain with L being the location of the outer boundaries along each axis. $R_{\text{diam}}/\Delta x$ denotes the grid number assigned inside the semimajor diameter of the NS. λ_0 is the gravitational wavelength of the initial configuration. (See Ref. [31] for models with nonspinning BHs.)

Model	l_c	l_f	$\Delta x/M_0$	$R_{\text{diam}}/\Delta x$	L/λ_0
2H-Q2M135a75	4	4	0.0471	90.8	2.386
1.5H-Q2M135a75	4	4	0.0426	87.7	2.417
H-Q2M135a75	4	4	0.0377	86.2	2.138
HB-Q2M135a75	4	4	0.0347	87.1	1.968
B-Q2M135a75	4	4	0.0324	86.7	1.837
2H-Q2M135a5	4	4	0.0471	90.8	2.378
1.5H-Q2M135a5	4	4	0.0426	87.7	2.410
H-Q2M135a5	4	4	0.0377	86.2	2.131
HB-Q2M135a5	4	4	0.0347	87.2	1.962
B-Q2M135a5	4	4	0.0324	86.7	1.831
2H-Q2M135a-5	4	4	0.0470	90.7	2.092
H-Q2M135a-5	4	4	0.0376	86.4	1.902
HB-Q2M135a-5	4	4	0.0347	87.1	1.962
B-Q2M135a-5	4	4	0.0324	86.7	1.831
2H-Q2M12a75	3	4	0.0583	84.7	1.476
H-Q2M12a75	3	4	0.0442	85.3	1.252
HB-Q2M12a75	3	4	0.0410	85.7	1.162
B-Q2M12a75	3	4	0.0389	84.2	1.102
2H-Q2M145a75	3	4	0.0461	85.2	1.166
H-Q2M145a75	3	4	0.0347	85.3	0.985
HB-Q2M145a75	3	4	0.0316	87.1	0.896
B-Q2M145a75	3	4	0.0292	87.1	0.829
2H-Q3M135a75	4	4	0.0367	85.5	2.084
1.5H-Q3M135a75	4	4	0.0326	84.0	1.986
H-Q3M135a75	4	4	0.0282	84.7	1.718
HB-Q3M135a75	4	4	0.0260	85.6	1.581
B-Q3M135a75	4	4	0.0235	87.9	1.431
2H-Q3M135a5	4	4	0.0353	88.9	1.997
1.5H-Q3M135a5	4	4	0.0326	84.0	1.980
H-Q3M135a5	4	4	0.0282	84.7	1.712
HB-Q3M135a5	4	4	0.0260	85.7	1.576
B-Q3M135a5	4	4	0.0243	85.3	1.471
HB-Q3M135a-5	4	4	0.0260	85.7	1.576
2H-Q3M145a75	3	4	0.0328	87.7	0.933
H-Q3M145a75	3	4	0.0250	87.4	0.760
HB-Q3M145a75	3	4	0.0234	86.6	0.712
B-Q3M145a75	3	4	0.0214	87.7	0.651
2H-Q4M135a75	4	4	0.0296	83.4	1.804
H-Q4M135a75	4	4	0.0223	84.5	1.450
HB-Q4M135a75	4	4	0.0203	86.5	1.319
B-Q4M135a75	4	4	0.0190	85.8	1.237
2H-Q4M135a5	4	4	0.0296	83.2	2.097
H-Q4M135a5	4	4	0.0219	85.9	1.548
HB-Q4M135a5	4	4	0.0205	85.5	1.448
B-Q4M135a5	4	4	0.0188	86.4	1.332
2H-Q5M135a75	3	5	0.0235	86.3	1.718
H-Q5M135a75	3	5	0.0180	86.2	1.314
HB-Q5M135a75	3	5	0.0167	86.3	1.224
B-Q5M135a75	3	5	0.0159	84.6	1.159

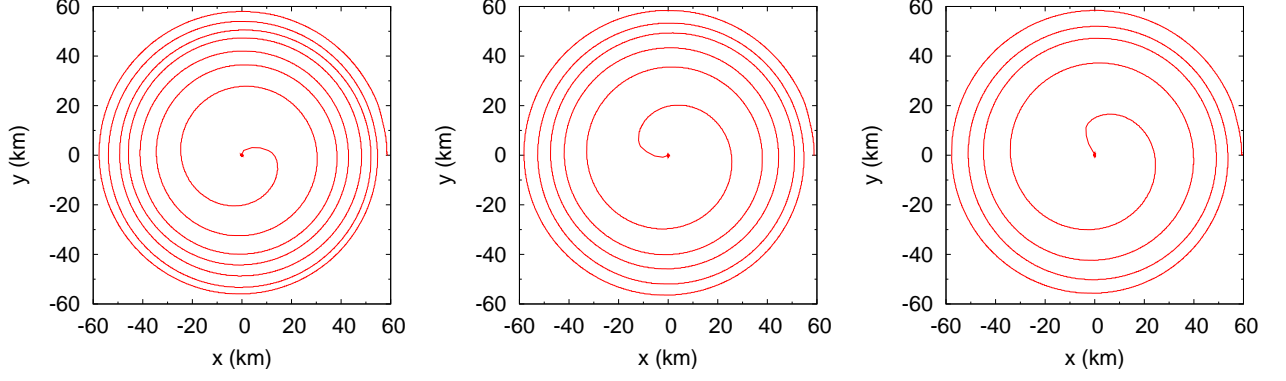


FIG. 1. Evolution of the orbital separation $x_{\text{sep}}^i = x_{\text{NS}}^i - x_{\text{BH}}^i$ of binaries with $(Q, M_{\text{NS}}) = (2, 1.35M_{\odot})$ and HB EOS. The left, middle, and right panels show the results with the prograde BH spin $a = 0.5$, zero BH spin $a = 0$, and retrograde BH spin $a = -0.5$, respectively.

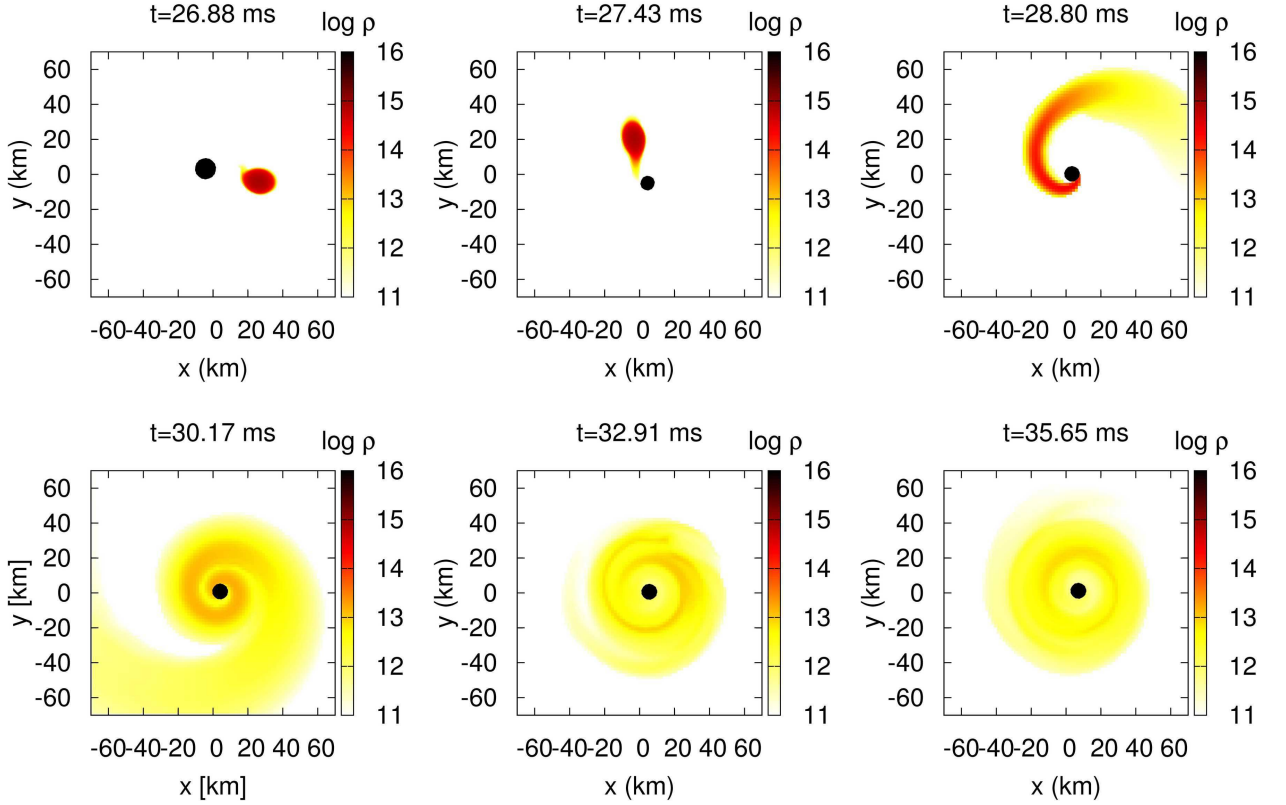


FIG. 2. Evolution of the rest-mass density profile in units of g/cm^3 and the location of the AH on the equatorial plane for model HB-Q3M135a75. The filled circle denotes the region inside the AH. The color (gradational) panel on the right of each plot show $\log_{10}(\rho)$.

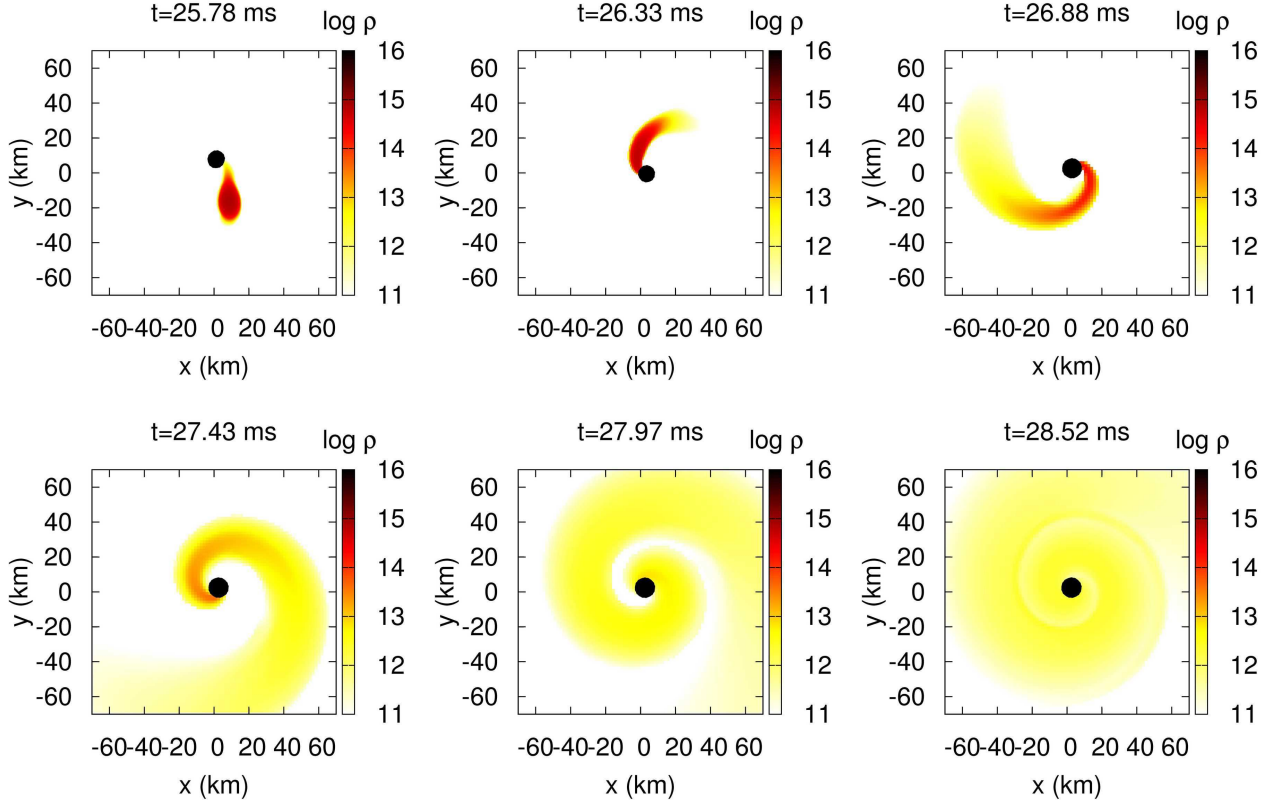


FIG. 3. The same as Fig. 2 but for model HB-Q3M135a5.

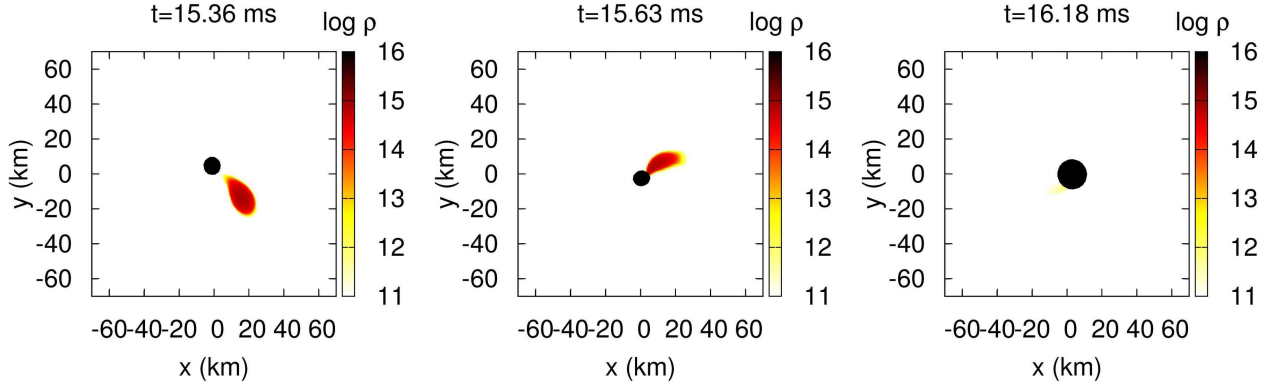


FIG. 4. The same as Fig. 2 but for model HB-Q3M135a-5.

plane at selected time slices for models HB-Q3M135a75, HB-Q3M135a5, and HB-Q3M135a-5 in Figs. 2–4, respectively. The NS is disrupted outside the ISCO in the $a > 0$ cases (Figs. 2 and 3) and forms a one-armed spiral structure with a large angular momentum. The material in the inner part of the spiral arm gradually falls onto the BH due to angular momentum transport via hydrodynamic torque in the spiral arm. The material with a sufficiently large specific angular momentum escapes the capture by the BH and forms an accretion disk, which survives for a time much longer than the dynamical time

scale \sim a few ms. We note that the prompt infall of the one-armed spiral structure onto the BH occurs from a relatively narrower region for $a = 0.5$ than for $a = 0.75$. The reason is that the inner edge of the spiral arm contacts the AH well before the arm becomes nearly axisymmetric due to a large radius of the AH and ISCO for $a = 0.5$. The infall of the disrupted material from a narrow region of the BH frequently occurs when the NS is tidally disrupted in a binary with a *high mass ratio*, whereas this is rare in a binary with a nonspinning BH because the NS is not disrupted in a high mass-ratio binary. This

difference in the merger process is well-reflected in gravitational waveforms (see Sec. IV E). By contrast, the NS is swallowed by the BH without tidal disruption, and essentially no material is left outside the ISCO for model HB-Q3M135a-5 (Fig. 4).

Note that the feature of the NS tidal disruption appears very weakly not only for model HB-Q3M135a-5 but also for model HB-Q3M135 ($a = 0$) because the mass ratio $Q = 3$ is so high that the tidal effect is less important for the nonspinning BH with the typical NS radius ~ 11 – 12 km. The enhancement of the tidal effect by a prograde BH spin results primarily from the decrease of the BH ISCO radius [67]. In the Boyer-Lindquist coordinates, a Kerr BH has an ISCO with a smaller radius than a Schwarzschild BH by a factor of $\geq 1/6$, depending on a for a prograde orbit: The ISCO radius approximately halves when the BH spin increases from $a = 0$ to 0.75 . On the other hand, the orbital separation at the onset of mass shedding depends only weakly on the BH spin in the Boyer-Lindquist coordinates [80–82]. This decrease of the ISCO radius enhances the possibility for the disrupted material to escape capture by the BH and to form a more massive remnant disk than in the nonspinning BH case. The retrograde BH spin plays an opposite role; the ISCO radius of the Kerr BH increases by a factor of 1 – 1.5 for a retrograde orbit, and hence, the tidal effect is less important in the merger process.

Before closing this subsection, we estimate the degree of (undesired) orbital eccentricity in our simulations to assess the circularity of the orbital motion. For this purpose, we compute the evolution of the gauge-invariant orbital angular velocity $\Omega(t)$, which is defined from the $(l, m) = (2, 2)$ mode of Ψ_4 by

$$\Omega(t) = \frac{1}{2} \frac{|\Psi_4(l = m = 2)|}{|\int \Psi_4(l = m = 2) dt|}. \quad (32)$$

The evolution of the orbital angular velocity in our simulation agrees with that derived from the Taylor-T4 formula in the inspiral phase within a small modulation, typically $\Delta\Omega/\Omega \lesssim 5\%$, which is equivalent to the orbital eccentricity of $\lesssim 3\%$. This amount of orbital eccentricity is as small as that observed in the nonspinning BH case with a low mass ratio $Q = 2$ [31].

B. Global properties of the disk

The mass of the remnant disk reflects the significance of NS tidal disruption in a clear way because the disk formation is a result of tidal disruption. A massive disk is formed if tidal disruption of the NS occurs far outside the ISCO. If the mass shedding starts in the vicinity of or inside the ISCO, only a small portion of the mass is left outside the AH. The material is not left outside the AH when the mass shedding does not occur before the BH swallows the NS, and the merger of a BH-NS binary may be indistinguishable from that of a BH-BH binary except for very small tidal corrections to the inspiral. Thus, the

mass of a remnant disk is a reliable indicator of the degree of tidal disruption.

Figure 5 plots the time evolution of the rest mass located outside the AH, $M_{r > r_{\text{AH}}}$, for $Q = 2$ and 3 with different nondimensional BH spin parameters $a = 0.75, 0.5, 0,$ and -0.5 . In both plots, $M_{\text{NS}} = 1.35M_{\odot}$ and HB EOS are adopted. We note that the results revised from the previous work [31] are plotted for $a = 0$. The dependence of $M_{r > r_{\text{AH}}}$ on a for HB EOS found here is similar to those for other EOSs. We set the time origin to be an approximate merger time t_{merger} . These plots indicate that the mass of the material left outside the AH relaxes to a quasisteady value for $t - t_{\text{merger}} \gtrsim 3$ – 4 ms, and the relaxed value increases monotonically as the BH spin increases from retrograde to prograde. This is consistent with the decrease of the BH ISCO radius with the increase of its spin, as described in Sec. IV A. In particular, the remnant disk mass at ≈ 10 ms after the merger is $\gtrsim 0.1M_{\odot}$ for all the EOSs with $(Q, a) = (2, \geq 0.5)$ and $(\leq 4, 0.75)$, as shown in Table V, and $\gtrsim 0.05M_{\odot}$ for $(Q, a) = (3, 0.5)$, irrespective of the EOS. The formation of such a massive disk may be encouraging for the BH-NS binary merger hypothesis of a short-hard GRB. For the $a = -0.5$ cases, by contrast, massive accretion disks of $\gtrsim 0.01M_{\odot}$ are not expected to be formed as merger remnants even for $Q = 2$ unless the EOS is extremely stiff (the NS radius is ≈ 15 km). This fact indicates that the retrograde BH spin is unfavorable for producing a central engine of a short-hard GRB.

The prograde BH spin enhances the disk formation dramatically for a BH-NS binary with a *high mass ratio*, for which the disk mass is very low when the BH is nonspinning. We plot the time evolution of $M_{r > r_{\text{AH}}}$ for $Q = 4$ and 5 with different EOSs in Fig. 6. In both plots, $M_{\text{NS}} = 1.35M_{\odot}$ and $a = 0.75$ are adopted. Figure 6 clearly shows that a massive accretion disk is formed for $Q = 4$ and 5 if the BH has a prograde spin of $a = 0.75$. Namely, the formation of a massive accretion disk is universal for the merger of a BH-NS binary with a mass ratio of $Q \lesssim 5$ as far as $a \sim 0.75$ and $M_{\text{NS}} = 1.35M_{\odot}$ (equivalently, $M_{\text{BH}} \lesssim 6.75M_{\odot}$). Note that a heavy BH of $M_{\text{BH}} \gtrsim 5M_{\odot}$ is predicted to be realistic as an astrophysical consequence of the stellar evolution with solar metallicity [83] (see, e.g., Ref. [84] for a population synthesis study) and hence as a possible progenitor of the short-hard GRB.

For more quantitative discussion, we plot the disk mass estimated at ≈ 10 ms after the merger for all the models with $Q = 2$ and for models with $(Q, a) = (3, \geq 0)$ as a function of the NS compactness, \mathcal{C} , in Fig. 7. Numerical values of $M_{r > r_{\text{AH}}}$ are shown in Table V, as well as other quantities associated with the merger remnants. For any fixed value of a , a negative correlation between $M_{r > r_{\text{AH}}}$ and \mathcal{C} is found to hold in Fig. 7. This correlation indicates that the NS with a larger compactness is less subject to tidal deformation and disruption than the NS with a smaller compactness for any fixed value of a . This correlation is expected from the nature of a tidal force as

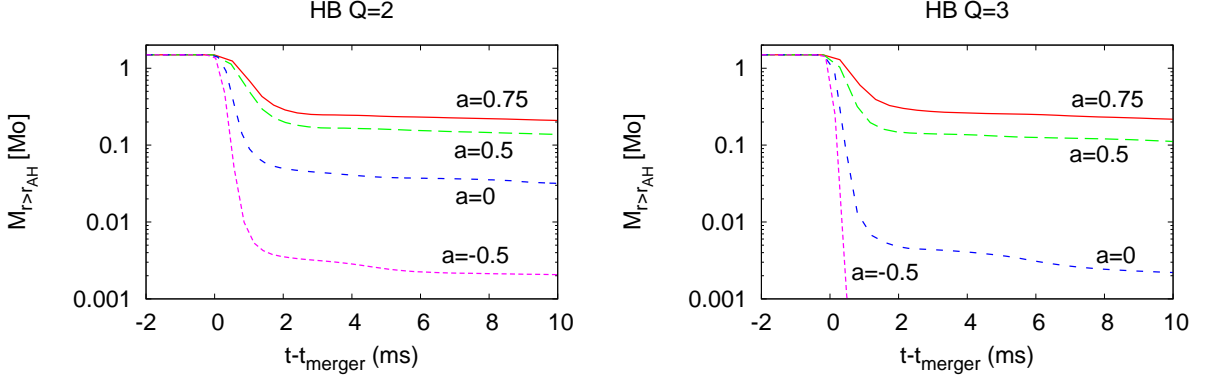


FIG. 5. Evolution of the rest mass of the material located outside an AH of the BH, $M_{r>r_{\text{AH}}}$. The left and right panels show the results for $Q = 2$ and 3 , respectively. In both plots, $M_{\text{NS}} = 1.35M_{\odot}$ and HB EOS are adopted. The results revised from the previous paper [31] are plotted for $a = 0$.

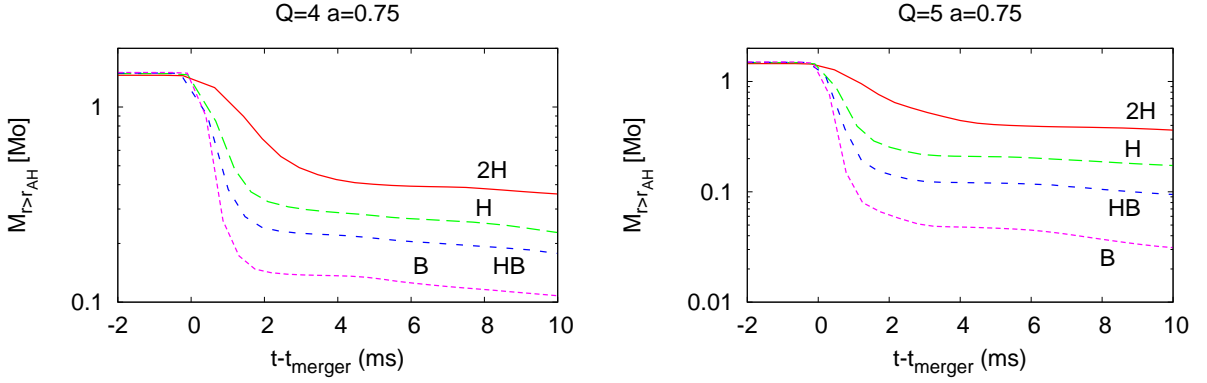


FIG. 6. The same as Fig. 5 but for different models $Q = 4$ (left) and 5 (right). In both plots, $M_{\text{NS}} = 1.35M_{\odot}$ and $a = 0.75$ are adopted.

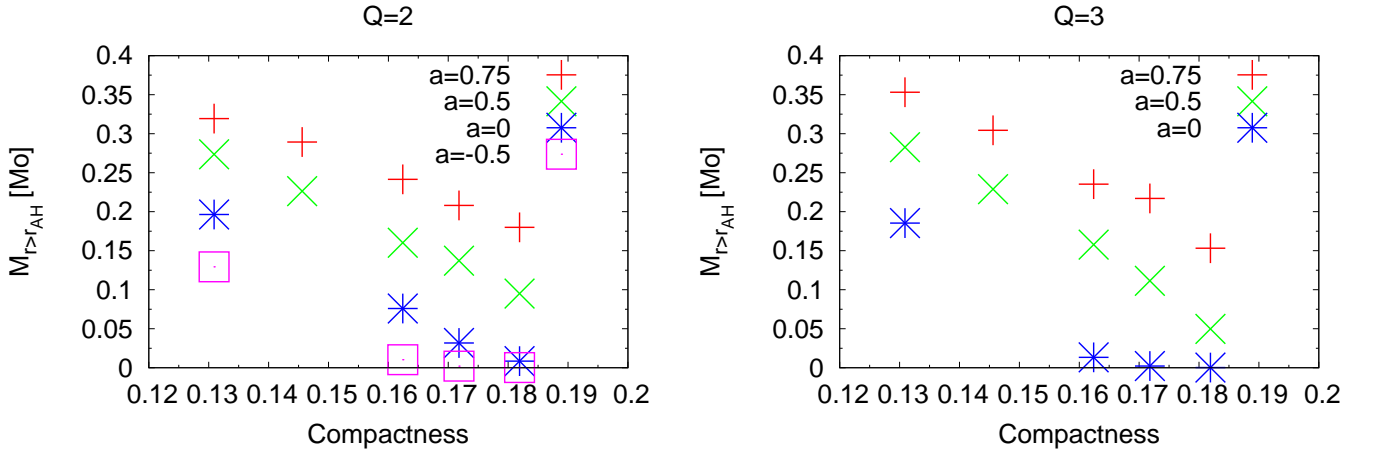


FIG. 7. The disk mass $M_{r>r_{\text{AH}}}$ at ≈ 10 ms after the onset of the merger as a function of the NS compactness \mathcal{C} . The left and right panels show the results for $Q = 2$ (left) and 3 (right). The results revised from the previous work [31] are plotted for $a=0$.

a finite-size effect, as found in the study of nonspinning BH-NS binaries [31]. On the other hand, Fig. 7 again shows that the prograde BH spin increases the disk mass for any fixed value of \mathcal{C} . A remarkable fact is that the disk mass does not decrease steeply to a value of $\ll 0.1M_\odot$ as the compactness increases for binaries with $(Q, a) = (\leq 3, \geq 0.5)$. We expect that the coalescence of a BH-NS binary with $(Q, a) = (\leq 3, \geq 0.5)$ may always produce a remnant disk of $\gtrsim 0.01M_\odot$ within a plausible range of the NS compactness, $\mathcal{C} \lesssim 0.2$, although it is possible only if $\mathcal{C} \lesssim 0.18$ for $(Q, a) = (2, 0)$ and $\mathcal{C} \lesssim 0.16$ for $(Q, a) = (2, -0.5)$ or $(3, 0)$.

The dependence of the disk mass on the NS compactness is different for different values of the mass ratio. We plot in Fig. 8 the disk mass as a function of the NS compactness as in Fig. 7, but for $a = 0.75$ and 0.5 . This figure shows that the disk mass depends more strongly on \mathcal{C} when the mass ratio, Q , is larger. The disk mass is larger for smaller values of Q when the EOS is soft and $\mathcal{C} \gtrsim 0.16$, except for HB-Q2M135a75 and HB-Q3M135a75, for which the disk masses depend only weakly on Q . This dependence on Q is expected from the comparison between the mass-shedding radius, r_{shed} , and the ISCO radius, r_{ISCO} ,

$$\frac{r_{\text{shed}}}{r_{\text{ISCO}}} \propto \mathcal{C}^{-1} Q^{-2/3}, \quad (33)$$

where we assume Newtonian gravity for simplicity. This relation states that a larger amount of mass can escape the capture by the BH and can form an accretion disk when Q is small because the mass shedding sets in at relatively more distant orbit. However, the disk mass may be larger for larger values of Q when the EOS is stiff as $\mathcal{C} \lesssim 0.15$ for $a \geq 0.5$ and $2 \lesssim Q \lesssim 5$. This should be ascribed to the redistribution process of the specific angular momentum of the NS to the disrupted material and to subsequent behavior of the material (such as collision of the fluid elements in spiral arms). This feature suggests that a binary with a larger value of Q , say $Q \gtrsim 6$, possibly form a massive remnant disk of $\gtrsim 0.1M_\odot$ and could be a progenitor of a short-hard GRB if the EOS is stiff and the BH has a large spin $\gtrsim 0.5$.

To clarify the dependence of the disk mass on the BH spin, we plot the disk mass as a function of a in Fig. 9. The EOS (and, equivalently, \mathcal{C}) is the same for each plot. Again, we find a monotonic and steep increase of the disk mass as the increase of a for the fixed EOS and mass ratio. The enhancement of the disk mass by a prograde spin is more dramatic for the compact NS (for the soft EOS). For example, the difference in the disk mass between the cases of $a = 0.75$ and -0.5 is only by a factor of ~ 3 when $Q = 2$ and 2H EOS is adopted. This low amplification is natural because tidal disruption of a large NS occurs at an orbit far enough from the ISCO for a substantial amount of the disrupted material to escape the capture by the BH irrespective of a and because at such a large orbital separation the spin-orbit coupling effect is relatively weak. On the other hand, a few-orders-of-

magnitude amplification of the disk mass is seen when $Q = 2$ and HB EOS is adopted.

Finally, we comment on a possible unbound outflow. To estimate the rest mass of unbound material, we compute

$$M_{\text{ub}} \equiv \int_{r > r_{\text{AH}}} \rho_* H(-u_t - 1) d^3x, \quad (34)$$

where $H(x)$ is a step function. Here, the material with $u_t < -1$ should be considered to have an unbound orbit. We find that M_{ub} can be larger than $0.01M_\odot$ at ≈ 10 ms after the merger for the stiff EOS like 2H and H, and $a \geq 0$. However, M_{ub} does not approach a constant value and rather continues to decrease. Therefore, it is unclear whether M_{ub} estimated at 10 ms after the merger can really become unbound or not, and we do not show the precise values of M_{ub} . When the EOS is not stiff, M_{ub} is negligible within the accuracy of our simulations.

C. Structure of the remnant disk

The structure of the remnant disk and its time evolution process depend on the mass ratio of the binary. We plot the rest-mass density profile at ≈ 5 and 10 ms after the onset of the merger for binaries with $a = 0.75$, HB EOS, and different values of Q in Fig. 10. The left column of Fig. 10 is plotted for ≈ 5 ms after the onset of the merger and shows that the dense material of $\rho \gtrsim 10^9 \text{ g/cm}^3$ always extends to $\gtrsim 400$ km. The spiral arm always spreads to a far region irrespective of EOSs, as far as the tidal disruption results in a massive disk. These plots also suggest that the accretion disk for a large value of Q —say, $Q = 5$ —keeps a nonaxisymmetric structure in the vicinity of the remnant BH at this time. This feature is qualitatively the same for binaries with other EOSs. When Q is small as ~ 2 , the accretion disk becomes nearly axisymmetric in ≈ 5 ms after tidal disruption because the dynamical time scale of the system (which is proportional to the BH mass) is shorter for a smaller value of Q . Also, because the ISCO radius of the BH is smaller, the maximum rest-mass density, ρ_{max} , of the disk (which should be approximately proportional to the inverse square of the BH mass) reaches a higher value on average in time for a smaller value of Q . It should be noted that the difference in ρ_{max} comes primarily from the difference in the radius and not from the difference in the disk mass, which do not vary by an order of magnitude for $a = 0.75$ and $Q = 2$ – 5 . This difference in the nonaxisymmetric structure results in different features of gravitational waves (see Sec. IV E).

The middle and right columns of Fig. 10 plot snapshots at ≈ 10 ms after the onset of the merger. At this time, nonaxisymmetric structures are not as significant as those at ≈ 5 ms after the onset of the merger because the accretion disk settles toward an approximately stationary state in the vicinity of the BH. The maximum values of the rest-mass density, ρ_{max} , in the accretion

TABLE V. Several key quantities for the merger remnants for $M_{\text{NS}} = 1.35M_{\odot}$. All the quantities are estimated at ≈ 10 ms after the approximate merger time $t = t_{\text{merger}}$. $M_{r>r_{\text{AH}}}$ is the rest mass of the disk surrounding the BH; because the accretion is still ongoing due to the hydrodynamic angular momentum transport process, the listed values only give approximate masses of the long-lived accretion disks, which survive for a time longer than the dynamical time scale \sim a few ms. C_e and C_p are the circumferential radii of the AH along the equatorial and meridional planes, respectively. $C_e/4\pi$ and $M_{\text{BH,c}}$ denote approximate masses of the remnant BH. $M_{\text{irr,f}}$ is the irreducible mass of the remnant BH, and a_f is the nondimensional spin parameter of the remnant BH estimated from C_p/C_e . a_{f2} and a_{f1} are also the nondimensional spin parameters, estimated from the quantities on the AH and approximate conservation laws, respectively. We note that the values associated with the remnant BH for model B-Q2M135a75 (with an asterisk) are evaluated at ≈ 5 ms after the onset of the merger because the BH area decreases by $\gtrsim 1\%$ at ≈ 10 ms after the onset of the merger and the error becomes large.

Model	$M_{r>r_{\text{AH}}}[M_{\odot}]$	$C_e/4\pi M_0$	$M_{\text{BH,c}}/M_0$	$M_{\text{irr,f}}/M_0$	C_p/C_e	a_f	a_{f2}	a_{f1}
2H-Q2M135a75	0.32	0.913	0.915	0.789	0.807	0.87	0.87	0.95
1.5H-Q2M135a75	0.29	0.918	0.920	0.785	0.794	0.89	0.89	0.95
H-Q2M135a75	0.24	0.927	0.929	0.783	0.780	0.91	0.90	0.94
HB-Q2M135a75	0.21	0.933	0.934	0.783	0.772	0.91	0.91	0.94
B-Q2M135a75	0.18	0.937*	0.938	0.790*	0.778*	0.91*	0.91*	0.93
2H-Q2M135a5	0.27	0.925	0.926	0.825	0.843	0.81	0.81	0.84
1.5H-Q2M135a5	0.23	0.935	0.936	0.831	0.840	0.82	0.81	0.84
H-Q2M135a5	0.17	0.945	0.946	0.837	0.836	0.82	0.82	0.84
HB-Q2M135a5	0.14	0.951	0.952	0.840	0.832	0.83	0.83	0.84
B-Q2M135a5	0.095	0.959	0.960	0.846	0.830	0.83	0.83	0.84
2H-Q2M135a-5	0.13	0.961	0.962	0.931	0.954	0.48	0.48	0.50
H-Q2M135a-5	0.010	0.985	0.986	0.950	0.948	0.51	0.51	0.52
HB-Q2M135a-5	0.0021	0.985	0.986	0.952	0.950	0.50	0.50	0.51
B-Q2M135a-5	2×10^{-4}	0.983	0.984	0.952	0.952	0.49	0.49	0.50
2H-Q3M135a75	0.35	0.927	0.927	0.807	0.815	0.86	0.86	0.90
1.5H-Q3M135a75	0.30	0.931	0.934	0.811	0.815	0.86	0.86	0.90
H-Q3M135a75	0.24	0.939	0.943	0.820	0.818	0.85	0.85	0.91
HB-Q3M135a75	0.22	0.941	0.943	0.812	0.805	0.87	0.87	0.90
B-Q3M135a75	0.15	0.949	0.951	0.824	0.812	0.86	0.86	0.89
2H-Q3M135a5	0.28	0.939	0.940	0.858	0.874	0.74	0.74	0.77
1.5H-Q3M135a5	0.23	0.946	0.948	0.862	0.871	0.75	0.75	0.78
H-Q3M135a5	0.16	0.955	0.957	0.867	0.866	0.76	0.76	0.78
HB-Q3M135a5	0.11	0.961	0.963	0.871	0.864	0.77	0.77	0.78
B-Q3M135a5	0.050	0.969	0.971	0.877	0.862	0.77	0.77	0.79
HB-Q3M135a-5	$< 10^{-4}$	0.986	0.987	0.973	0.980	0.32	0.32	0.33
2H-Q4M135a75	0.36	0.937	0.938	0.825	0.828	0.84	0.84	0.87
H-Q4M135a75	0.23	0.948	0.951	0.831	0.823	0.84	0.84	0.88
HB-Q4M135a75	0.18	0.953	0.956	0.833	0.821	0.85	0.85	0.88
B-Q4M135a75	0.11	0.960	0.963	0.837	0.817	0.85	0.85	0.88
2H-Q4M135a5	0.28	0.950	0.951	0.879	0.891	0.70	0.70	0.72
H-Q4M135a5	0.085	0.970	0.973	0.890	0.880	0.73	0.73	0.74
HB-Q4M135a5	0.024	0.976	0.979	0.894	0.878	0.74	0.74	0.75
B-Q4M135a5	0.0034	0.978	0.980	0.896	0.878	0.74	0.74	0.75
2H-Q5M135a75	0.36	0.946	0.947	0.838	0.835	0.82	0.82	0.85
H-Q5M135a75	0.17	0.960	0.963	0.844	0.827	0.84	0.84	0.86
HB-Q5M135a75	0.095	0.966	0.970	0.848	0.824	0.84	0.84	0.86
B-Q5M135a75	0.031	0.972	0.975	0.851	0.821	0.85	0.85	0.87

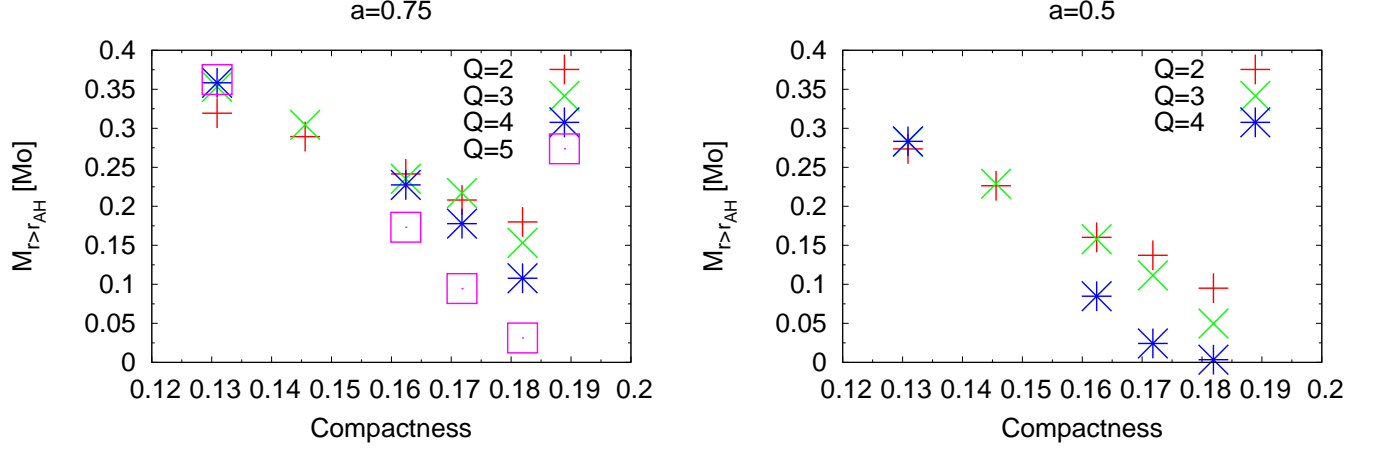


FIG. 8. The same as Fig. 7 but for $a = 0.75$ and $a = 0.5$ with $Q = 2-5$.

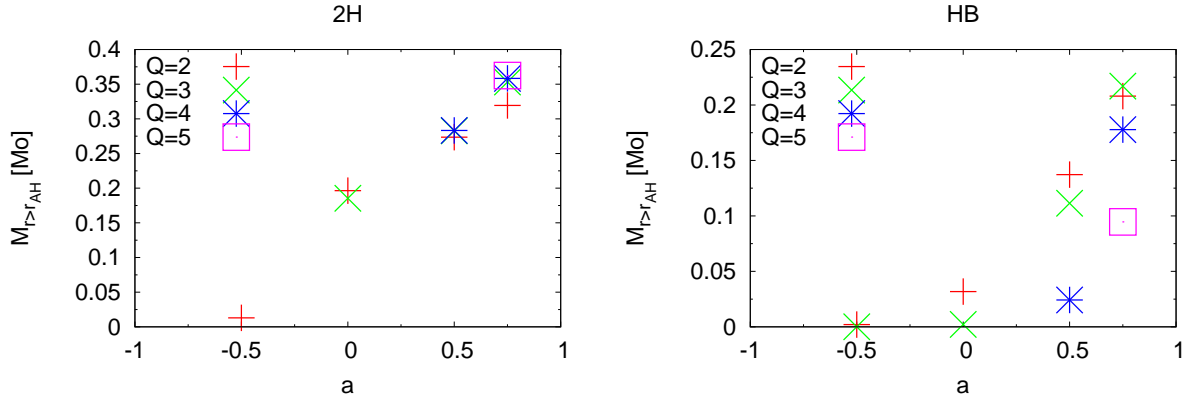


FIG. 9. The disk mass, $M_{r>r_{AH}}$, at ≈ 10 ms after the onset of the merger as a function of the nondimensional spin parameter of the BH a for models with $M_{NS} = 1.35M_{\odot}$. The left and right panels show the results for models with the 2H and HB EOSs, respectively. The results revised from the previous work [31] are plotted for $a = 0$.

disk are still higher for a smaller value of Q . Indeed, the right column of Fig. 10 shows that smaller values of Q result in producing a wider region with $\rho > 10^{12} \text{ g/cm}^3$. By contrast, the disk for $Q = 5$ does not have such a high-density region. The smaller density may be unfavorable to be the short-hard GRB model.

The size of a region where $\rho > 10^{10} \text{ g/cm}^3$ coincides approximately among four models with different values of Q and is always $\sim 100 \text{ km}$. Furthermore, the middle column suggests that the region of $\rho > 10^8 \text{ g/cm}^3$ extends to larger distances when Q is larger. We plot the radial distribution of ρ along x and y axes for these models in Fig. 11. Note that low-density regions near the origin are inside the BH. These plots show that ρ_{max} is systematically higher for the binary with a smaller value of Q . These also show that the location of the isodensity surface of $\rho = 10^{10} \text{ g/cm}^3$ approximately coincides among different values of Q . Taking these facts into account, we conclude that a typical profile of $\rho(r)$ is steeper for smaller values of Q in the vicinity of the BH. A region of $\gtrsim 100 \text{ km}$ away from the BH, where the profile $\rho(r)$ shows relatively shallow decrease and $\lesssim 10^{10} \text{ g/cm}^3$, corresponds to the tail component, as is seen in the middle column of Fig. 10.

D. Properties of the remnant BH

Table V shows that masses and nondimensional spin parameters of the remnant BHs depend weakly on the adopted EOSs. The mass of the remnant BH tends to become large as the EOS softens for fixed values of (Q, M_{NS}, a) for the case in which tidal disruption of the NS occurs. The reason for this is that the tidal disruption occurs near the ISCO, and then the BH swallows a large amount of the NS mass when the EOS is soft. Exceptionally, the mass of the BH becomes slightly larger for H and HB EOSs than for B EOS for binaries with $(Q, a) = (2, -0.5)$. The reason for this is that the remnant disk masses are small as $\lesssim 0.01M_{\odot}$ for these cases and the amount of the energy radiated by gravitational waves primarily determines the final state (for more compact NSs, the radiated energy is larger because a closer inspiral orbit is achieved). The spin angular momentum of the remnant BH $S_{\text{BH},f}$ shows similar behavior to that of the BH mass. The situation becomes complicated for a spin parameter of the remnant BH defined by $a_f = S_{\text{BH},f}/M_{\text{BH},f}^2$; the competition between the mass and angular momentum losses from the system makes the dependence of the nondimensional spin parameter of the remnant BH on the EOS very weak. For comparison, a_{f1} and a_{f2} defined in Sec. III B are also shown in Table V. As is found in our previous work [31], a_f and a_{f2} agree with each other within the error of $\Delta a = 0.003$. By contrast, a_{f1} does not agree well with the other two estimates, as is found in another previous work of ours [29], particularly when the massive remnant disk is formed and/or the mass of the BH is small: the maximum er-

ror is $\Delta a \approx 0.08$. Taking into account the fact that the agreement between $C_e/4\pi$ and $M_{\text{BH},f}$ is always better than 0.5%, a possible reason for this discrepancy is that Eq. (31) systematically underestimates the angular momentum of the disk. Hereafter, we only refer to a_f as the nondimensional spin parameter of the remnant BH.

The nondimensional spin parameter of the remnant BH depends strongly on the initial spin parameter, a , and the mass ratio, Q . Approximate values of the nondimensional spin parameter of the remnant BH, a_f , are shown in Fig. 12 as a function of the initial BH spin parameter, a . We also plot lines obtained by a linear fitting of data for $Q = 2$ and 3 of the following form,

$$a_f = 0.32a + 0.66 \quad (Q = 2), \quad (35)$$

$$a_f = 0.43a + 0.54 \quad (Q = 3). \quad (36)$$

The relation for $Q = 3$ agrees approximately with the results reported in Refs. [28, 85] within an error of $\lesssim 5\%$, and the agreement becomes better for a larger value of a . Figure 12 and these relations show that a_f is an approximately linear function of a . In a zeroth approximation, the slope and intercept of the linear relation denote the contribution from the initial BH spin angular momentum, S_{BH} , and the orbital angular momentum of the binary, J_0 , respectively. The larger slope for a larger value of Q is explained by a larger contribution from the spin of the initial BH of mass $M_{\text{BH}} = QM_{\text{NS}}$ to the spin of the remnant BH of mass $M_{\text{BH},f} \sim (1 + Q)M_{\text{NS}}$. These predict the value of the slope to be $Q^2/(1 + Q)^2$. However, the slope obtained by numerical simulations is smaller by $\sim 25\text{--}30\%$ than this predicted slope, because the amount of angular momenta redistributed to the remnant disk and extracted by gravitational waves become larger for a larger value of a . The fitting function also suggests that the merger of an extremely spinning BH of $a = 1$ and a NS with an irrotational velocity field results in a remnant BH with $a_f \approx 0.98$ for BH-NS binaries with $Q = 2$ and 3 and hence never forms an overspinning BH, i.e., a BH with $a_f > 1$. Furthermore, the results for $Q = 4$ shown in Table V also suggest $a_f \approx 0.97$ for the merger of an extremely spinning BH and an irrotational NS. These results give a circumstantial support for cosmic censorship conjecture [86]. Whether $a_f \lesssim 0.98 (< 1)$ is an universal consequence of a general BH-NS binary merger or not should be confirmed by simulations of higher mass-ratio binary mergers, in particular, with (nearly) extremal BH spin.

From these typical values of a_f and $M_{\text{BH},f}$, we can estimate typical frequencies of quasinormal modes (hereafter QNM) f_{QNM} of the remnant BH by a fitting formula [87]

$$f_{\text{QNM}}M_{\text{BH},f} \approx \frac{1}{2\pi} [1.5251 - 1.1568(1 - a)^{0.1292}]. \quad (37)$$

We plot these values in Fig. 13. They are in good agreement with those of the ringdown waveforms, if the QNM is excited after the merger.

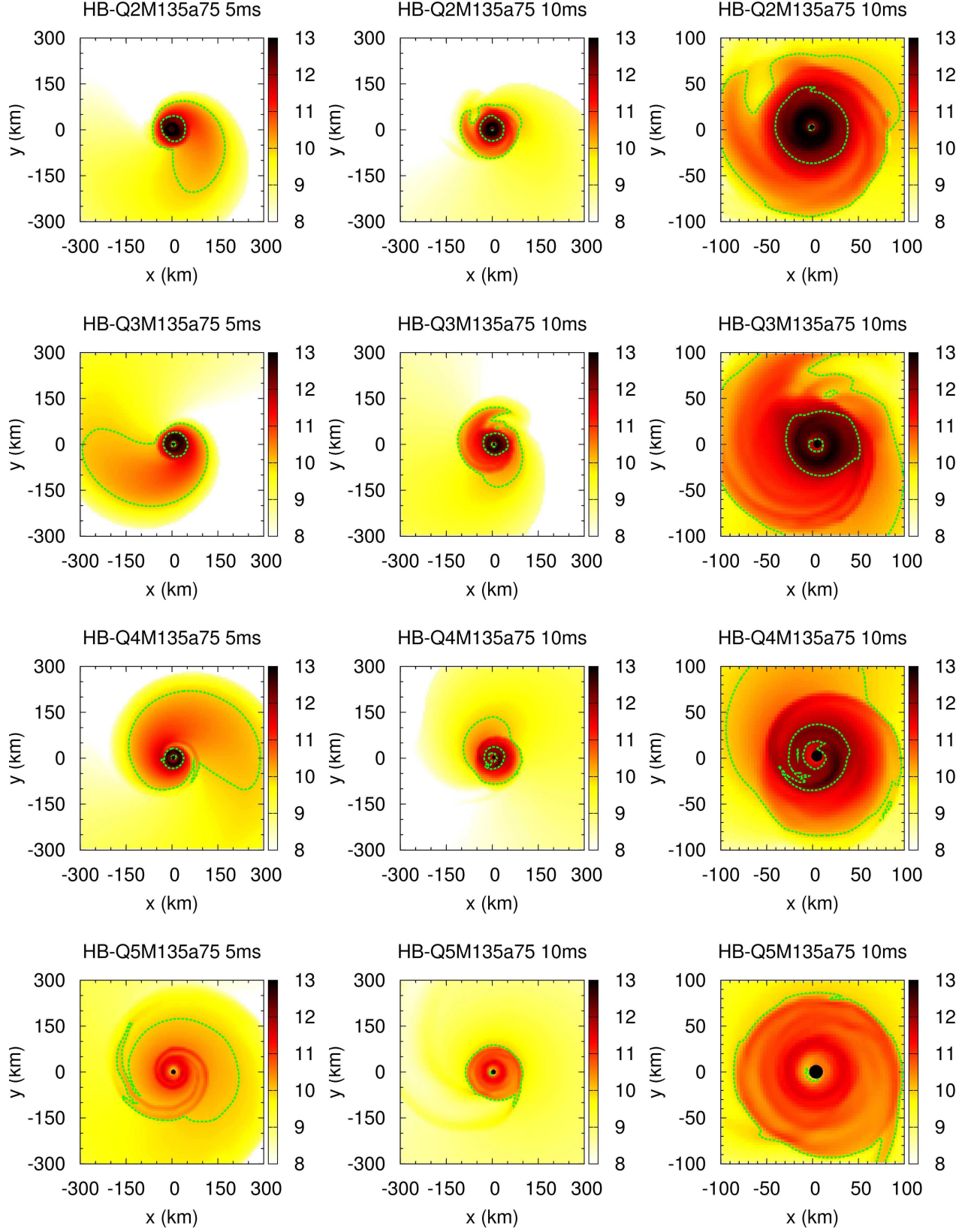


FIG. 10. The same as Fig. 2 with contour curves for $\rho = 10^{10}$ and 10^{12}g/cm^3 plotted. In all the plots, HB EOS and $a = 0.75$ are adopted. The first, second, third, and fourth rows are for $Q = 2, 3, 4,$ and 5 , respectively. The left column plots the snapshots at 5 ms after the onset of the merger. The middle column plots the snapshots at 10 ms after the onset of the merger, and the right column plots close-ups of the middle column.

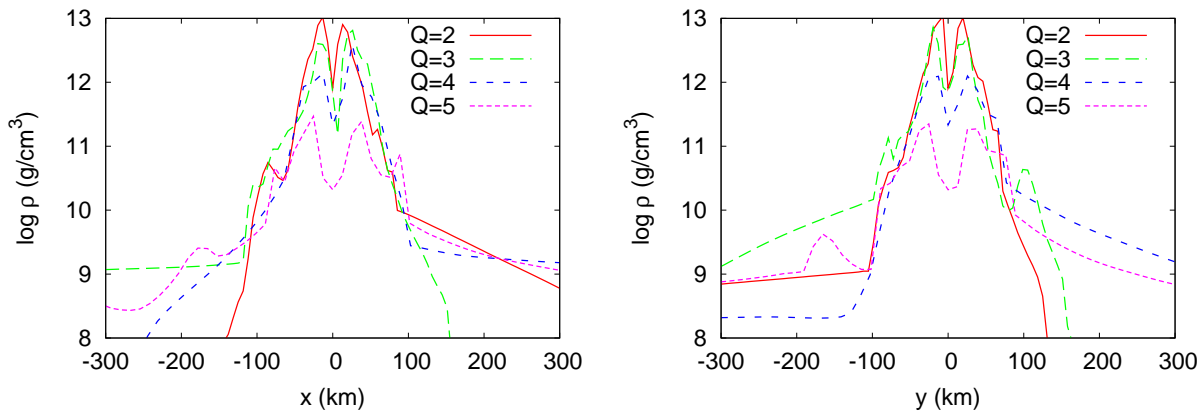


FIG. 11. Radial distribution of the rest-mass density at 10 ms after the onset of the merger for different values of Q . The left and right panels show the distribution along the x and y axes, respectively. In both plots, $(M_{\text{NS}}, a) = (1.35M_{\odot}, 0.75)$ and HB EOS are adopted.

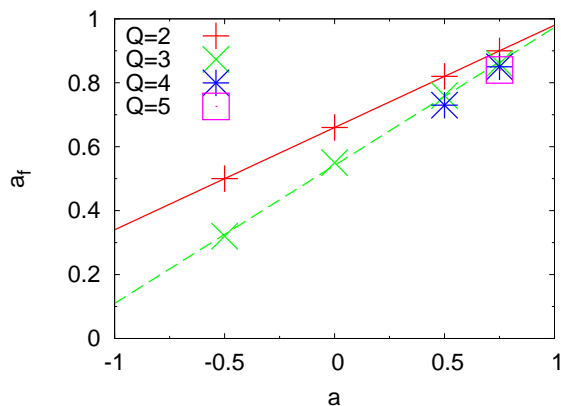


FIG. 12. The typical nondimensional spin parameters of the remnant BH a_f as a function of the initial BH spin parameter a . The solid lines are obtained by a linear fitting of the data for $Q = 2$ and $Q = 3$.

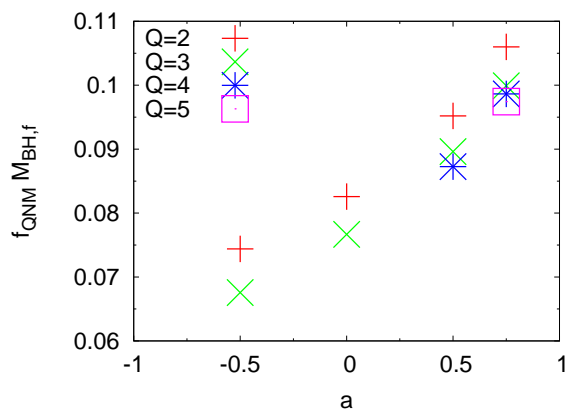


FIG. 13. The typical QNM frequency of the remnant BH normalized by its mass $f_{\text{QNM}} M_{\text{BH},f}$.

E. Gravitational waveforms

In this section, we show $(l, m) = (2, 2)$, plus-mode gravitational waveforms h_+ for selected models obtained in this study, as well as the waveform for models obtained in our previous simulations [31]. We plot all the waveforms for an observer along the z axis as a function of the approximate retarded time

$$t_{\text{ret}} = t - D - 2M_0 \ln(D/M_0). \quad (38)$$

The amplitude of the waveforms is normalized as Dh_+/m_0 or we show physical amplitude observed at a hypothetical distance $D = 100$ Mpc along the z axis. Gravitational waveforms calculated in the Taylor-T4 formula are plotted together in the figures to validate the waveforms obtained in our numerical simulations during the inspiral phase. Numerical waveforms during 2–3 initial cycles deviate from ones obtained from the Taylor-T4 formula in all the cases due to the lack of an approaching velocity in the initial data. This deficit is ascribed to insufficient modeling of the quasiequilibrium state and improvement in the future is important to obtain more accurate gravitational-wave templates [88, 89]. Our waveforms also deviate from the Taylor-T4 waveforms in the late inspiral phase due to a physical reason, which we describe below. Comparisons between waveforms obtained from simulations with different grid resolutions are shown in the Appendix .

Figure 14 shows the gravitational waveforms for binaries with HB EOS, $(Q, M_{\text{NS}}) = (3, 1.35M_{\odot})$ but with different BH spin parameters, $a = 0.75, 0.5, 0,$ and -0.5 . This figure shows that the time to the merger, to which we refer approximately as the time at which the maximum gravitational-wave amplitude is achieved, for $\Omega_0 m_0 = 0.030$ becomes longer by ≈ 10 ms as the increase of the BH spin within the range concerned here. This difference in the merger time owes primarily to the spin-orbit interaction described in Sec. IV A, and this

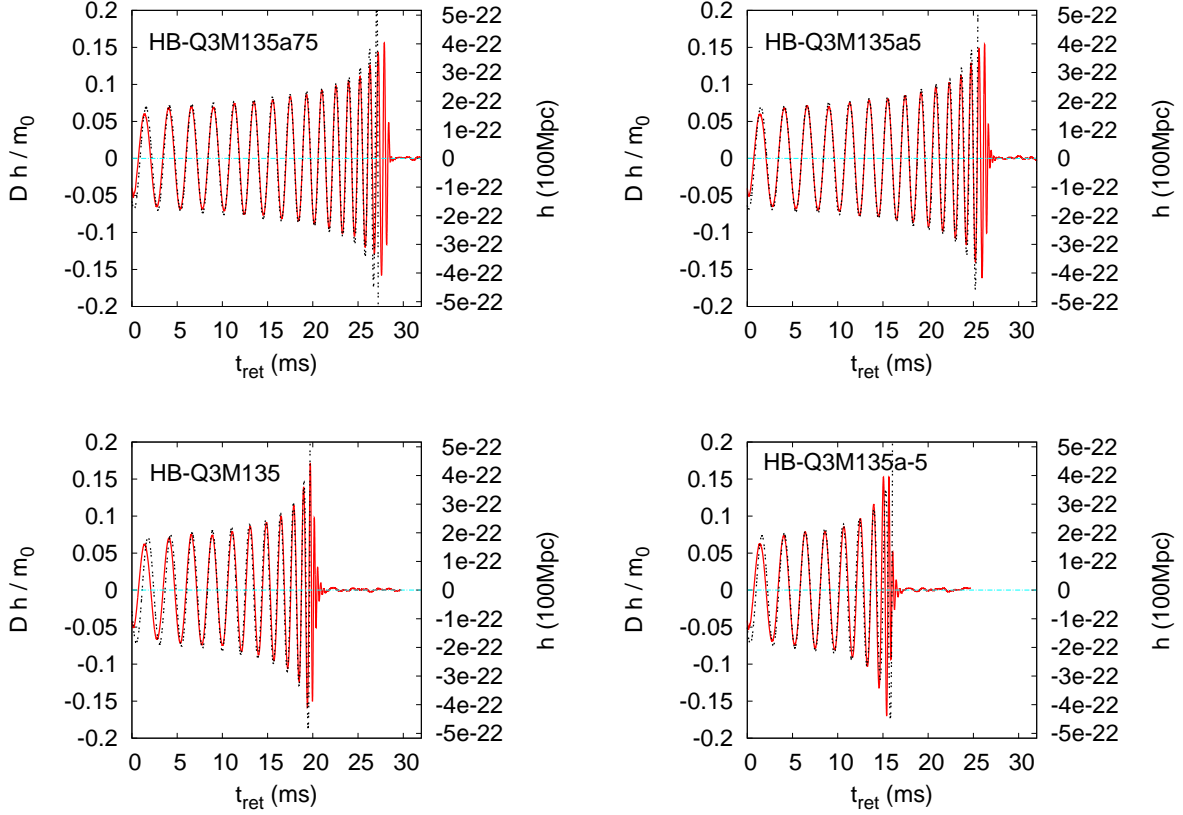


FIG. 14. $(l, m) = (2, 2)$, plus-mode gravitational waves for models HB-Q3M135a75, HB-Q3M135a5, HB-Q3M135, and HB-Q3M135a-5. All the waveforms are shown for an observer located along the z axis (the axis of rotation) and plotted as a function of a retarded time. The left axis denotes the amplitude normalized by the distance from the binary D and the total mass m_0 . The right axis denotes the physical amplitude of gravitational waves observed at a hypothetical distance 100 Mpc. The dotted curves denote the waveform calculated by the Taylor-T4 formula.

behavior is qualitatively the same for binaries with any EOS. The numerical and Taylor-T4 waveforms agree well with each other during an inspiral phase for all the cases.

For the prograde BH spin cases, the Taylor-T4 formula does not track the evolution for ~ 0.5 inspiral orbit just before the merger. The Taylor-T4 amplitude departs from that of numerical relativity and even diverges. Accordingly, the number of gravitational-wave cycles differs by as much as unity between the numerical and Taylor-T4 waveforms. The difference in the number of cycles is larger for higher mass-ratio binaries with prograde BH spins. We show the waveforms for binaries with $(Q, M_{\text{NS}}, a) = (4, 1.35M_{\odot}, 0.75)$ and with $(Q, M_{\text{NS}}, a) = (5, 1.35M_{\odot}, 0.75)$ for 2H, H, HB, and B EOSs in Figs. 15 and 16, respectively. The deviation is clear for H, HB, and B EOSs in both figures. This difference indicates that the phase evolution predicted by the Taylor-T4 formula is not sufficient to model the last inspiral phase of a coalescing binary with the high mass ratio of $Q \gtrsim 3$ and the prograde BH spin of $a \gtrsim 0.5$.

For the retrograde BH spin case (the bottom right panel of Fig. 14), the phase evolution deviates between the numerical and Taylor-T4 waveforms in the last orbit

before the merger. This deviation may be partly ascribed to the small number of orbits in our simulation but appears to be primarily ascribed to a larger angular velocity, or equivalently a larger PN parameter, Ωm_0 , at the last orbit for a retrograde BH spin. Thus, the Taylor-T4 formula seems to be again insufficient for modeling the retrograde BH spin cases.

Figure 14 also shows that the gravitational waveform in the merger stage depends strongly on the BH spin. For a binary with $(Q, a) = (3, 0.75)$, gravitational waves show a sudden decrease in the amplitude at $t_{\text{ret}} \approx 27$ ms, which is a clear signature of tidal disruption. Gravitational waves associated with the ringdown of a remnant BH are absent due to the phase cancellation by nearly axisymmetric accretion of the disrupted material. This feature is consistent with the formation of a massive remnant disk, which is described in Sec. IV B, for the prograde BH spin. For binaries with $(Q, a) = (3, \leq 0)$, on the other hand, gravitational waves end up with ringdown waveforms associated with the remnant BHs because the tidal effect is very weak throughout the merger. In these circumstances, gravitational waves do not show strong signatures of tidal deformation and disruption of the NS.

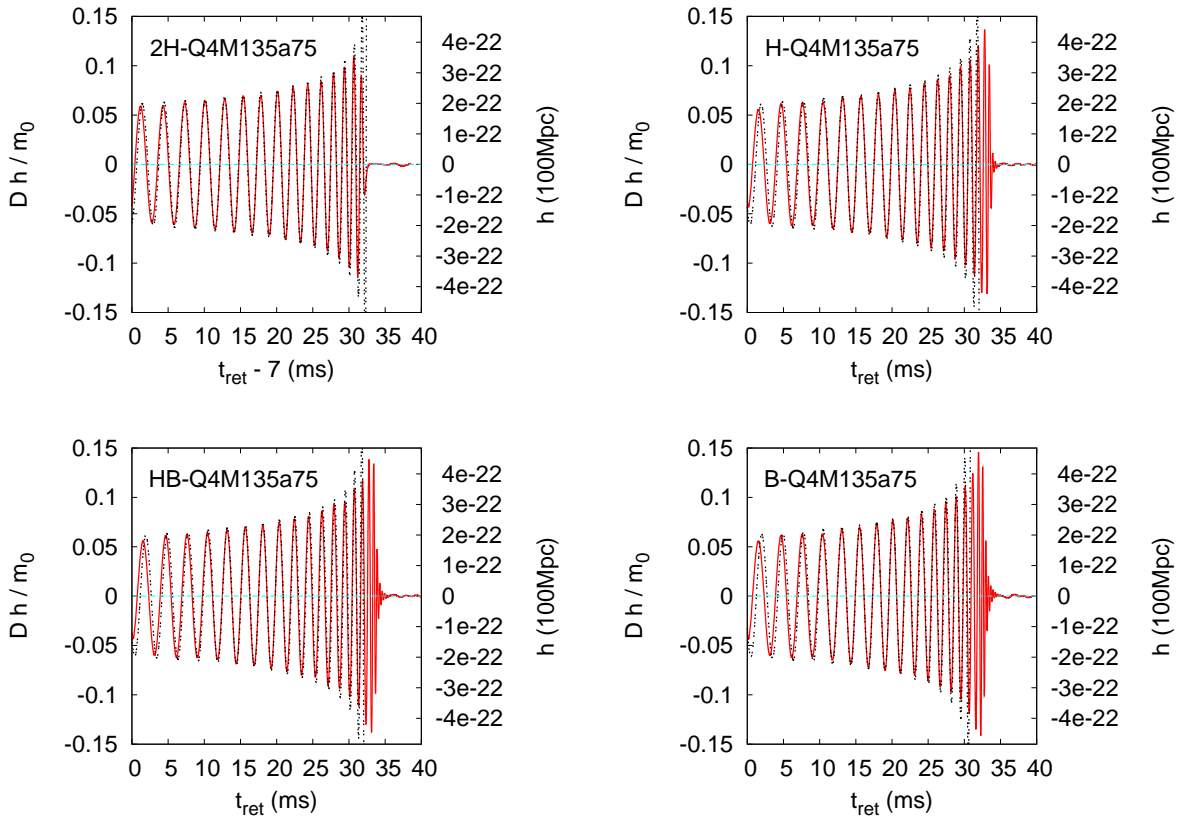


FIG. 15. The same as Fig. 14 but for models 2H-Q4M135a75, H-Q4M135a75, HB-Q4M135a75, and B-Q4M135a75.

Gravitational waves for a binary with $(Q, a) = (3, 0.5)$ show a qualitatively new feature (the top right panel of Fig. 14). In this case, a ringdown waveform of the remnant BH is seen in the final stage, although the NS is tidally disrupted and the disk mass is larger than $0.1M_{\odot}$. Namely, both tidal disruption of the NS and excitation of a QNM of the remnant BH occur in a compatible manner. The same feature is also found for a binary with a high mass ratio and a prograde BH spin, i.e., $(Q, a) = (\geq 4, 0.75)$, shown in Figs. 15 and 16 except for 2H EOS, with which the NS is disrupted at a fairly distant orbit. These waveforms are often seen for BH-NS binaries with a heavy BH (or a high mass ratio) with the prograde BH spin, which results in the NS tidal disruption, and is never seen for BH-NS binaries with $Q = 2$ or high mass-ratio binaries with nonspinning BHs.

The ratio of the areal radius of the remnant BH to the NS radius, R_{NS} , is intimately related to the different excitation degree of the QNM between low and high mass-ratio binaries in the presence of NS tidal disruption [90, 91]. Schematic pictures of merger processes are depicted in Fig. 17. If tidal disruption does not occur, the NS is simply swallowed by the BH and excites a QNM, as shown in the middle panel of Fig. 17. If tidal disruption occurs in a binary with a low mass ratio, the disrupted material spreads around the BH to soon form a nearly

axisymmetric disk. Approximately speaking, this occurs if the BH areal radius is smaller than the NS radius, as is shown in the left panel of Fig. 17. Thus, the NS tidal disruption has a strong effect to suppress the excitation of a QNM through the phase cancellation in the low mass-ratio binary. However, the situation is different in a high mass-ratio binary. Whereas the disrupted material forms an axisymmetric accretion disk around the BH in a sufficiently long time duration, the accretion just after the merger does not proceed in an axisymmetric way in high mass-ratio binaries, such as $Q = 4$, except for the extremely stiff EOS. This is because the BH radius for $Q = 4$ approximately doubles that for $Q = 2$, and hence, the disrupted material takes longer time to spread around the BH. In other words, the NS material accretes onto the BH coherently even after the tidal disruption, as is shown in the right panel of Fig. 17, because the BH radius is so large that the disrupted material cannot fully cover the BH surface before the BH swallows a large portion of the material. In the exceptional 2H EOS case, tidal disruption occurs sufficiently far outside the BH due to the large radius of the NS, and hence, the disrupted material is able to spread around the BH to form a nearly axisymmetric accretion disk before the prompt infall. Therefore, the QNM of a remnant BH is not excited for 2H EOS.

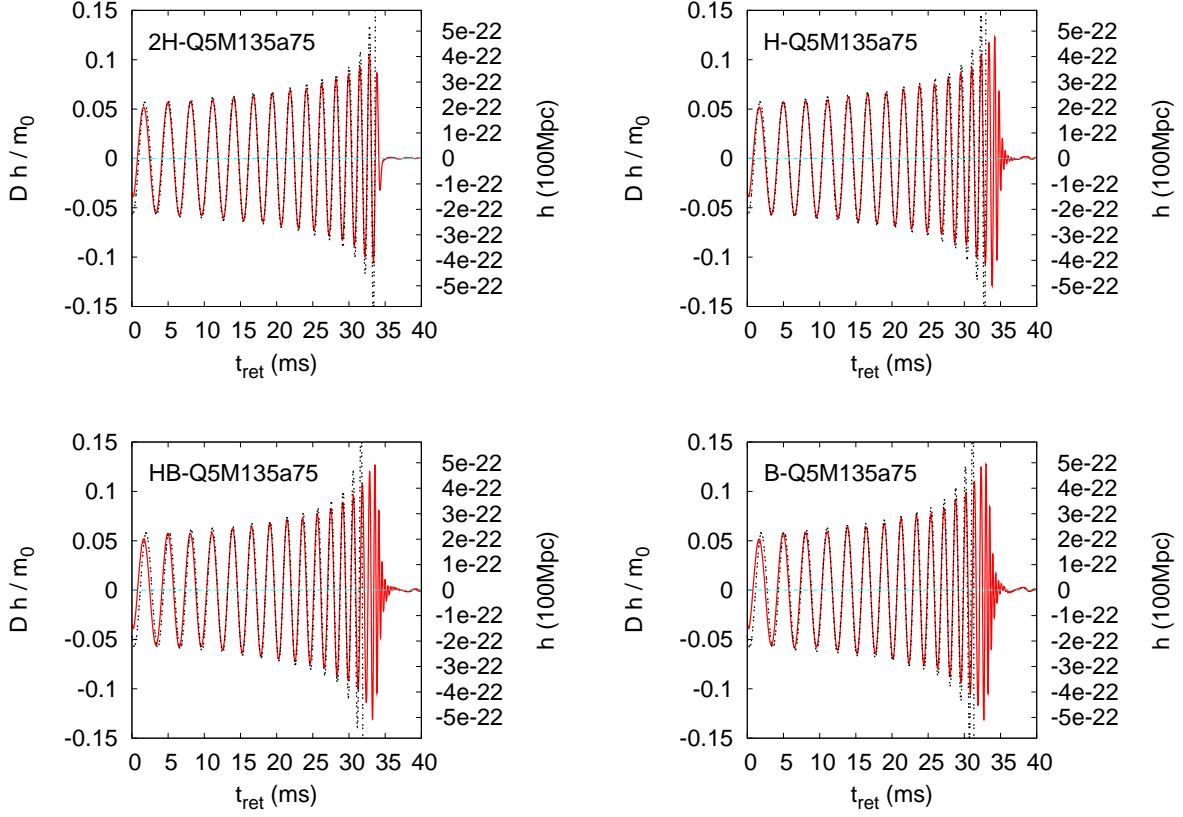


FIG. 16. The same as Fig. 14 but for models 2H-Q5M135a75, H-Q5M135a75, HB-Q5M135a75, and B-Q5M135a75.

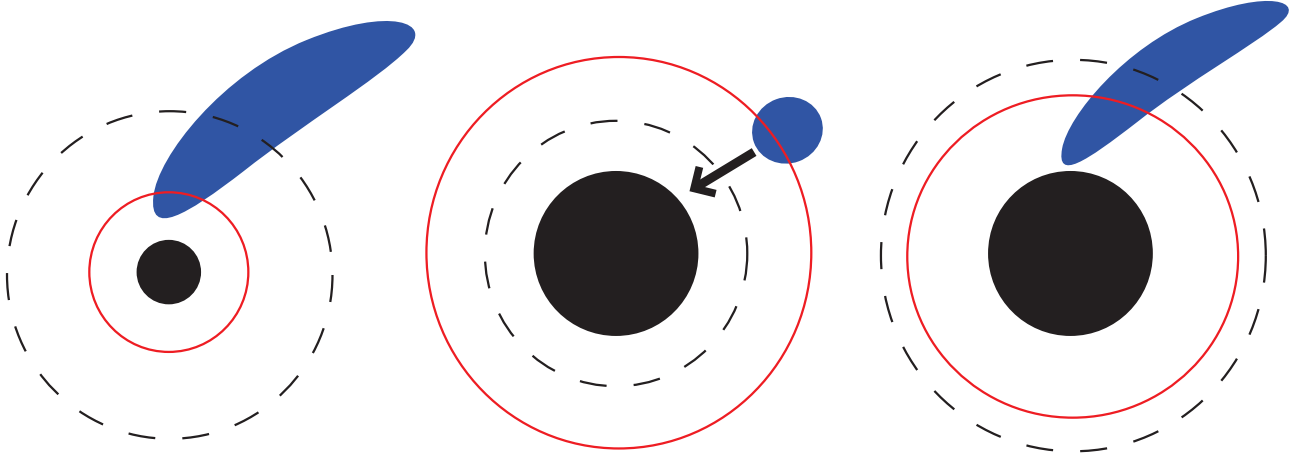


FIG. 17. Schematic pictures for three types of the merger process. The solid filled circle denotes the BH, the distorted ellipsoid denotes the NS, the solid circle is the location of the ISCO, and the dashed circle is the location of the radius at which the tidal disruption occurs. Left: the NS is tidally disrupted, and the spatial extent of the disrupted material is larger than or as large as that of the BH. Middle: the NS is not tidally disrupted. Right: the NS is tidally disrupted, and the spatial extent of the disrupted material is smaller than that of the BH.

F. Gravitational-wave spectrum

spectrum as a sum of each Fourier component of two

Key features of gravitational waves are reflected in the Fourier spectrum. In this paper, we define the Fourier

independent polarizations of the $(l, |m|) = (2, 2)$ mode as

$$\tilde{h}(f) = \sqrt{\frac{|\tilde{h}_+(f)|^2 + |\tilde{h}_\times(f)|^2}{2}}, \quad (39)$$

$$\tilde{h}_A(f) = \int e^{2\pi ift} h_A(t) dt, \quad (40)$$

where A denotes two polarization modes, $+$ or \times . We show a nondimensional spectrum, $f\tilde{h}(f)$, observed at a hypothetical distance of 100 Mpc as a function of the gravitational-wave frequency, f (Hz), or a normalized amplitude, $f\tilde{h}(f)D/m_0$, as a function of a nondimensional frequency, fm_0 . The amplitude of gravitational waves, h_A , is given as the amplitude observed along the z axis, which is the most optimistic direction for the gravitational-wave detection. We note that the actual amplitude of gravitational waves depends on an angle locating the source in the sky and on an angle specifying the orientation of the orbital plane of the binary. The angular average of the effective amplitude is $\approx 0.4f\tilde{h}(f)$. We always exclude spurious radiation components for $t_{\text{ret}} \lesssim 0$ ms, using a step function of the retarded time as a window function.

To show the dependence of the gravitational-wave spectra on the BH spin parameter, we plot the spectra for models HB-Q2M135a75, HB-Q2M135a5, HB-Q2M135, and HB-Q2M135a-5 in the left panel of Fig. 18 and for models HB-Q3M135a75, HB-Q3M135a5, HB-Q3M135, and HB-Q3M135a-5 in the right panel of Fig. 18. In the early inspiral phase of $f \lesssim 1$ kHz, where the point-particle approximation works well, the amplitude of the gravitational-wave spectrum for a given frequency increases monotonically as a increases. This is a feature expected from the PN calculation and is explained by the spin-orbit interaction as follows: The power spectrum of gravitational radiation is written as

$$\frac{dE}{df} \propto [f\tilde{h}(f)]^2. \quad (41)$$

On the other hand, retaining only 1.5PN, the lowest-order spin-orbit interaction terms, Eqs. (4.10) and (4.14) of Ref. [79], derive the expression for this quantity as

$$\frac{dE}{df} = \frac{Q}{3(1+Q)^2} \frac{X^{5/2}}{\pi f^2} \left[1 + aX^{3/2} \left\{ \frac{5(4Q+3)}{3(1+Q)^2} \right\} \right]. \quad (42)$$

Thus, the effective amplitude, $f\tilde{h}(f)$, for a given frequency f increases monotonically as the BH spin parameter, a , increases in the inspiral phase.

Figure 19 plots the spectra for models 2H-Q2M135a75, H-Q2M135a75, HB-Q2M135a75, and B-Q2M135a75, for which only the EOS is different, and indicates that the amplitude in the early inspiral phase does not depend strongly on \mathcal{C} . This is because the finite-size effect of the NS does not play an important role in the early inspiral phase (but, see Refs. [93, 94]), as already found for nonspinning BH-NS binaries [31].

In the late inspiral phase of $1 \text{ kHz} \lesssim f \lesssim f_{\text{cut}}$, where f_{cut} is a characteristic frequency at which the spectrum starts damping exponentially (see below), the amplitude is significantly larger than the Taylor-T4 formula for the cases in which the NS is not disrupted. This is because the binaries in the inspiral and plunge after the NS enters the BH's ISCO emit gravitational waves in reality, whereas the Taylor-T4 formula does not take into account the motion inside the ISCO. In contrast to the spectrum calculated by the Taylor-T4 formula, which decreases steeply after the last inspiral phase, the amplitude obtained from the simulation depends only weakly on the gravitational-wave frequency in that phase, as far as the tidal disruption does not occur.

The most fruitful information of the NS comes from the gravitational-wave spectrum in the merger phase through the ‘‘cutoff frequency,’’ f_{cut} , which depends on the BH spin as well as the NS compactness [29, 31]. If the NS tidal disruption occurs, the spectrum damps at $f = f_{\text{tidal}} \sim 2\text{--}4$ kHz, which denotes the frequency at the tidal disruption and depends sensitively on physical parameters of the binary. In that case, gravitational waves for a higher frequency, $f \gtrsim f_{\text{cut}} \approx f_{\text{tidal}}$, are not emitted by the binary in the inspiral motion but only weakly by disrupted material. Because the disrupted material gradually spreads around the BH to form a nearly axisymmetric disk, the emission of gravitational waves is suppressed at the high frequency. Thus, the spectrum shows a relatively moderate damping around $f \approx f_{\text{cut}}$, which is closely related to the NS compactness through the tidal disruption. The spectra for binaries with $(Q, a) = (2, \geq 0)$ and $(3, \geq 0.5)$ in the left panel of Fig. 18 correspond to these cases. We see that the cutoff frequency, f_{cut} , for these models decreases as the BH spin parameter increases. This is ascribed to the decrease of the orbital frequency at the tidal disruption for a binary with the prograde BH spin. The enhancement of the effective centrifugal force by the spin-orbit interaction reduces the orbital frequency at the tidal disruption, f_{tidal} , although the orbital separation at the tidal disruption itself does not vary much even in the presence of the BH spin. If the tidal disruption does not occur during the merger, however, inspiral-like motion continues at higher frequencies near and even inside the ISCO until the BH swallows the NS. In this case, the spectrum amplitude depends only weakly on f in the frequency range $f \lesssim f_{\text{cut}}$ and damps for $f \gtrsim f_{\text{cut}}$, which is closely related to the QNM frequency of the remnant BH, f_{QNM} . The spectra for $(Q, a) = (2, -0.5)$ and $(3, \leq 0)$ in Fig. 18 show this feature. Note that the amplitude for model HB-Q3M135a-5 is smaller than for model HB-Q3M135 for the frequency range shown in Fig. 18 because tidal disruption does not play an important role, and Eq. (42) applies throughout the merger in both cases.

It is noteworthy that a prograde BH spin is favorable for the gravitational-wave detection in the inspiral phase and the estimation of f_{cut} in the merger phase because the prograde spin enhances the amplitude for a given

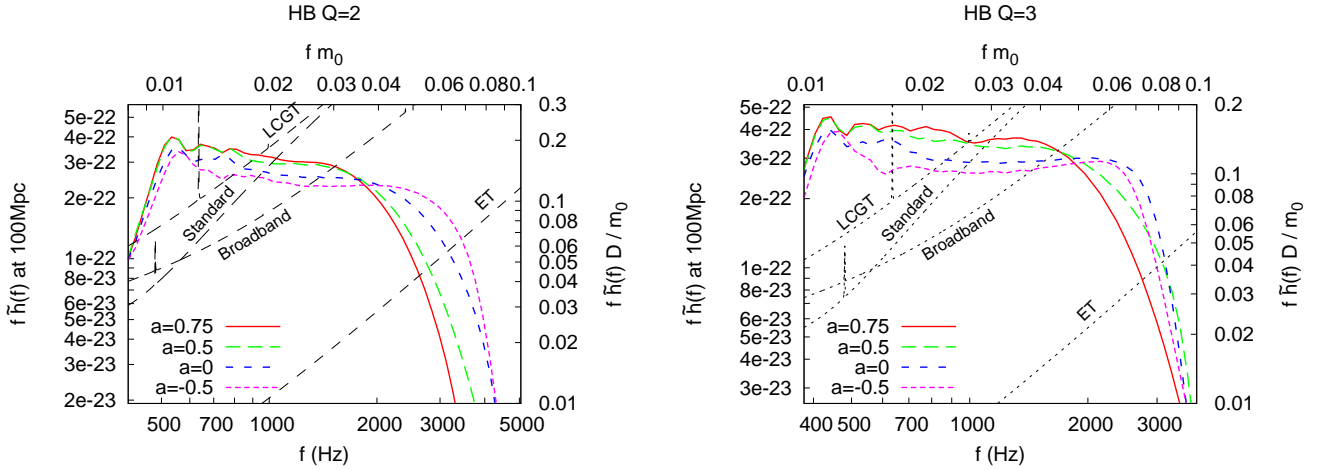


FIG. 18. Gravitational-wave spectra for BH-NS binaries with HB EOS, $M_{\text{NS}} = 1.35M_{\odot}$ and $a = 0.75, 0.5, 0,$ and -0.5 . The left and right panels show the spectra for $Q = 2$ and 3 , respectively. The upper axis denotes the normalized frequency, fm_0 , and the right axis denotes the normalized amplitude, $f\tilde{h}(f)D/m_0$. The bottom axis denotes the frequency, f , in Hz, and the left axis denotes the nondimensional amplitude of gravitational waves, $f\tilde{h}(f)$, observed at a hypothetical distance 100 Mpc from the binary along the z axis. The dashed curves are planned noise curves of the LCGT (“LCGT”), the Advanced LIGO optimized for $1.4M_{\odot}$ NS-NS detection (“Standard”), the Advanced LIGO optimized for the burst detection (“Broadband”), and the Einstein Telescope (“ET”) [92].

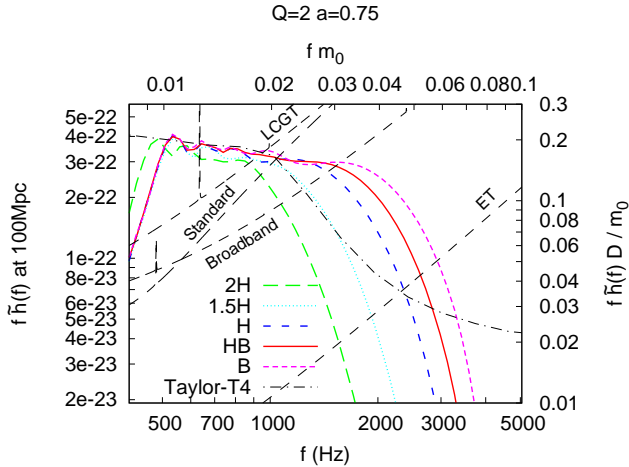


FIG. 19. The same as Fig. 18 but for $(Q, M_{\text{NS}}, a) = (2, 1.35M_{\odot}, 0.75)$ with 2H, H, HB, and B EOSs. The spectrum derived by the Taylor-T4 formula is also included.

frequency in the inspiral phase and decreases the cutoff frequency in the merger phase. Note that the most sensitive frequency range for ground-based detectors is $f \sim 10$ Hz–1 kHz, which is usually lower than f_{cut} . Thus, the features found here are encouraging for the gravitational-wave astronomy to become an important tool for investigating the NS radius and EOS.

The gravitational-wave spectra of binaries with high mass ratios show qualitatively different behavior for a high frequency. Figure 20 plots the gravitational-wave spectra obtained for models with $(Q, M_{\text{NS}}, a) = (4, 1.35M_{\odot}, 0.75)$ and $(5, 1.35M_{\odot}, 0.75)$. For these bina-

ries (except for the model with 2H EOS), both the NS tidal disruption and the excitation of a QNM of the remnant BH occur as is described in Sec. IV E. Hence, the gravitational spectrum has two characteristic frequencies, i.e., f_{tidal} and f_{QNM} , simultaneously. The spectra plotted in Fig. 20 indeed show such features. After the NS is tidally disrupted, the amplitude of the gravitational-wave spectrum shows a slow damp for $f \gtrsim f_{\text{tidal}} \approx 2$ kHz. Then, the spectrum damps steeply above the frequency of the QNM, $f \gtrsim f_{\text{QNM}} \approx 3$ kHz. A schematic figure of different spectra is depicted in Fig. 21, and the spectrum described in this paragraph corresponds to spectrum (iii) in this figure. This suggests that the cutoff frequency, f_{cut} , of a high mass-ratio binary is not determined by a unique physical process like NS tidal disruption or a ringdown of a remnant BH, as far as both of them occur.

To estimate the cutoff frequency quantitatively, we fit the gravitational-wave spectra by a function with seven free parameters of the form

$$\frac{f\tilde{h}_{\text{fit}}(f)D}{m_0} = \frac{f\tilde{h}_{3\text{PN}}(f)D}{m_0} e^{-(f/f_{\text{ins}})^{\sigma_{\text{ins}}}} + A e^{-(f/f_{\text{dam}})^{\sigma_{\text{dam}}}} [1 - e^{-(f/f_{\text{ins}2})^{\sigma_{\text{ins}2}}}], \quad (43)$$

where $\tilde{h}_{3\text{PN}}(f)$ is the Fourier spectrum calculated by the Taylor-T4 formula. The first term in Eq. (43) models the inspiral spectrum, and the second term models the merger and ringdown spectra. We determine seven free parameters f_{ins} , $f_{\text{ins}2}$, f_{dam} , σ_{ins} , $\sigma_{\text{ins}2}$, σ_{dam} , and A by the condition that the following weighted norm is minimized:

$$\sum_i \left\{ [f_i \tilde{h}_i(f_i) - f_i \tilde{h}_{\text{fit}}(f_i)] f_i^{1/3} \right\}^2. \quad (44)$$

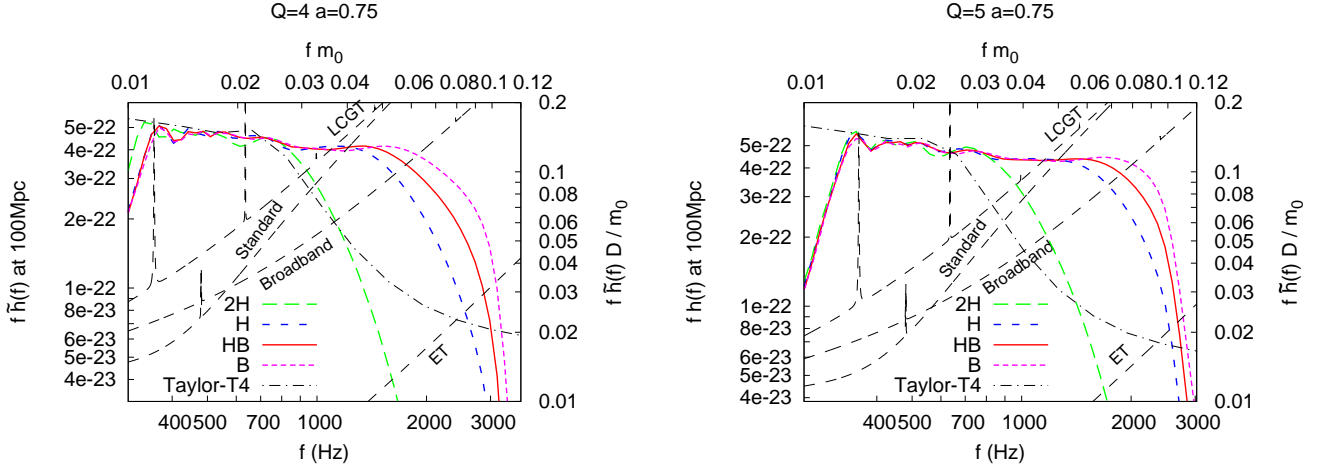


FIG. 20. The same as Fig. 18 but with the left panel for $(Q, M_{\text{NS}}, a) = (4, 1.35M_{\odot}, 0.75)$ and the right panel for $(5, 1.35M_{\odot}, 0.75)$ with 2H, H, HB, and B EOSs. The spectrum derived by the Taylor-T4 formula is also included.

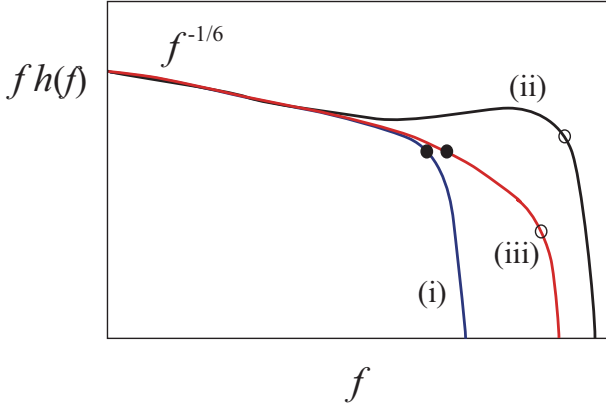


FIG. 21. A schematic figure of three types of gravitational-wave spectra. Spectrum (i) is for the case in which tidal disruption occurs far outside the ISCO, and spectrum (ii) is for the case in which tidal disruption does not occur. Spectrum (iii) is for the case in which tidal disruption occurs and the QNM is also excited. The filled and open circles denote f_{tidal} and f_{QNM} , respectively.

Here, i denotes the data point for the spectrum. In the previous works [29, 31], we identify f_{dam} in Eq. (43) with f_{cut} , which is most strongly correlated with the NS compactness for nonspinning BH-NS binaries [95]. In the present work, however, we obtain no strong correlation between f_{dam} (and the other parameters) and any parameter of physical importance, such as a or \mathcal{C} . The reason may be ascribed to the inadequacy of the functional form of Eq. (43), where the set of free parameters is degenerate to some extent. In particular, such a degeneracy is severe for a high mass-ratio binary due to two reasons. First, modeling an inspiral spectrum by the Taylor-T4 formula is inadequate for the late inspiral phase of a high mass-ratio binary due to the lack of information from the Taylor-T4 formula, as is described in Sec. IV E. Second,

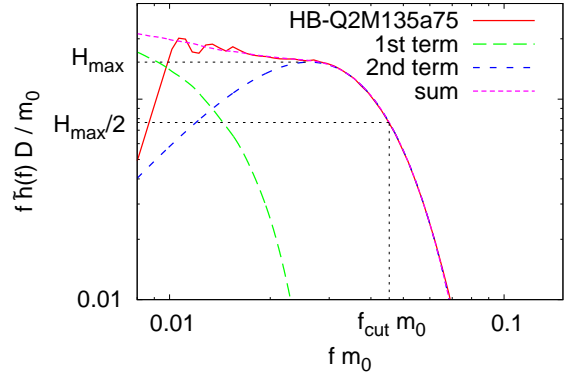


FIG. 22. The fitting for model HB-Q2M135a75. The long-dashed and middle-dashed curves show the first and second terms of Eq. (43), respectively. The short-dashed curve is the sum of these two terms.

there is no unique, physically motivated identification of f_{cut} when both the NS tidal disruption and the QNM excitation occur. (Fortunately, these degeneracies did not cause problems in the case of the nonspinning BH-NS binary with a low mass ratio [31].) To overcome these problems with the fitting procedure, we redefine f_{cut} as the higher one of two frequencies at which the second term in Eq. (43) takes a half value of its maximum. An example of this fitting procedure is shown in Fig. 22. In this figure, H_{max} corresponds to the maximum value of the second term in Eq. (43). We find that this definition of f_{cut} works well to read off the NS compactness from the gravitational-wave spectrum.

Figure 23 shows $f_{\text{cut}}m_0$ for spectra obtained for all binaries with $Q = 2$ as a function of the NS compactness, \mathcal{C} , in logarithmic scales. We also plot the typical QNM frequency of the remnant BH, f_{QNM} , which depends primarily on a of the initial BH for a fixed value of Q . For

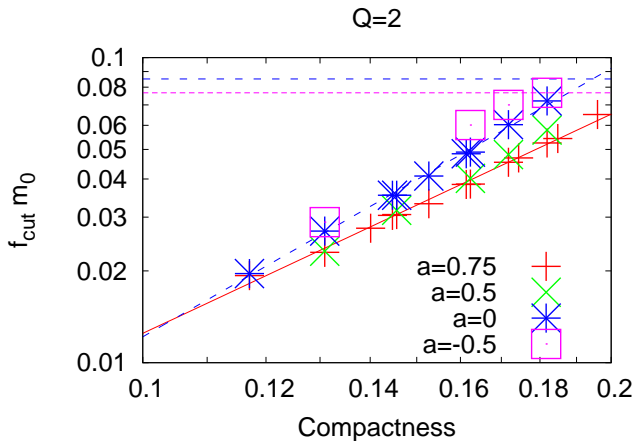


FIG. 23. The cutoff frequency times the total mass $f_{\text{cut}}m_0$ as a function of the NS compactness \mathcal{C} for $Q = 2$ binaries in logarithmic scales. The solid and dashed lines are obtained by linear fittings of data for $a = 0.75$ and $a = 0$, respectively. Horizontal lines denote the typical QNM frequencies of the remnant BHs. We note that $f_{\text{QNM}} > f_{\text{cut}}$ for $a = 0.75$ as long as $\mathcal{C} \leq 0.2$.

each value of a , we find that $f_{\text{cut}}m_0$ increases monotonically as \mathcal{C} increases, and an approximate power law holds as

$$\ln(f_{\text{cut}}m_0) \approx p(a) \ln \mathcal{C} + q(a) \quad (Q = 2), \quad (45)$$

where $p(a) (> 0)$ and $q(a)$ depend only on a , for any value of a when $Q = 2$. This monotonic relation between $f_{\text{cut}}m_0$ and \mathcal{C} suggests us a possibility to extract the compactness, \mathcal{C} , of a NS from the gravitational-wave observation. It is noteworthy that this relation includes only \mathcal{C} but neither M_{NS} nor R_{NS} independently. It should also be noted that the simple relation found here is a consequence of our choice for a common value of the adiabatic index of the core EOS, $\Gamma_2 = 3$ [31]. The increase of $f_{\text{cut}}m_0$ with the increase of \mathcal{C} indicates that a more compact NS is less subject to the BH tidal effect and disrupted at a closer orbit to the BH than a less compact NS is. The difference in $f_{\text{cut}}m_0$ due to the difference in a becomes clearer for larger values of \mathcal{C} , and conversely, $f_{\text{cut}}m_0$ depends only weakly on a if the compactness is as small as ≈ 0.12 . The weak dependence on a for the small values of \mathcal{C} is due to the fact that the effect of the BH spin at a distant orbit, at which the NS with a large radius is disrupted, is weak.

Figure 23 also shows that $p(a)$ is a decreasing function of a . More specifically we obtain the relations

$$\ln(f_{\text{cut}}m_0) = (2.92 \pm 0.06) \ln \mathcal{C} + (2.32 \pm 0.12) \quad (46)$$

for $a = 0$ [96] and

$$\ln(f_{\text{cut}}m_0) = (2.39 \pm 0.06) \ln \mathcal{C} + (1.11 \pm 0.11) \quad (47)$$

for $a = 0.75$ by a linear fitting. The decreasing nature of $p(a)$ is explained by the fact that the spin-orbit repulsive

force for the prograde BH spin, which reduces the orbital frequency at the NS tidal disruption, works efficiently for a close orbit and hence for the NS with a large value of \mathcal{C} . It is important that $p(a)$ is always larger than 1.5, which is expected from the analysis of the condition for the mass shedding,

$$\Omega m_0 \propto \frac{\mathcal{C}^{3/2}(1+Q)^{3/2}}{\sqrt{Q}}. \quad (48)$$

The large value of $p(a)$ is favorable for determining the NS compactness from the gravitational-wave observation because the dependence of f_{cut} on \mathcal{C} becomes stronger. Note that f_{cut} is always lower than the QNM frequency of the remnant BH for a realistic range of the compactness $\mathcal{C} \lesssim 0.2$ for $(Q, a) = (2, \gtrsim 0)$. If a is negative, on the other hand, f_{cut} for the binary with a compact NS of $\mathcal{C} \gtrsim 0.18$ may be determined by the QNM frequency, f_{QNM} , and it will be difficult to determine the NS compactness from the cutoff frequency.

Figure 24 shows the $f_{\text{cut}}m_0$ - \mathcal{C} relation of gravitational-wave spectra obtained for all binaries with $a = 0.75$ and $a = 0.5$. This figure, combined with Fig. 23, clearly indicates that the approximate power law of the form

$$\ln(f_{\text{cut}}m_0) = p(Q, a) \ln \mathcal{C} + q(Q, a) \quad (49)$$

holds for binaries of $\mathcal{C} \lesssim 0.2$ with $Q = 5$ as far as $a \sim 0.75$ and with $Q \leq 4$ as far as $a \sim 0.5$. The striking feature is that the cutoff frequency is lower than the QNM frequency of the remnant BH, f_{QNM} , for $(Q, a) = (\leq 4, 0.75)$ and for $(Q, a) = (\leq 3, 0.5)$ even if a QNM is excited. Accordingly, f_{cut} shows a strong correlation with \mathcal{C} . For $(Q, a) = (5, 0.75)$ and $(4, 0.5)$, f_{cut} is lower than f_{QNM} as far as $\mathcal{C} \lesssim 0.18$ and 0.17 , respectively, and, therefore, the strong correlation between f_{cut} and \mathcal{C} is found within this range. Although f_{cut} for the binary with a high mass ratio should not be considered as f_{tidal} due to the QNM excitation, monotonic relations between $f_{\text{cut}}m_0$ and \mathcal{C} gives us an opportunity to explore the NS radius and EOS. It should be noted that gravitational waves from a higher mass-ratio binary are more subject to the gravitational-wave detection due to the larger amplitude in the inspiral phase and the lower cutoff frequency. We again note that a massive BH of $M_{\text{BH}} \gtrsim 5M_{\odot}$ is an astrophysically realistic consequence of the stellar evolution [83, 84]. Taking these facts into account, we conclude that gravitational waves from the BH-NS binary are a promising tool to investigate the NS radius and EOS in the next decade.

G. Energy and angular momentum radiated by gravitational waves

Table VI lists the total energy $\Delta E/M_0$ and angular momentum $\Delta J/J_0$ radiated by gravitational waves. We estimate systematic errors in the estimation of ΔE and ΔJ to be $\sim 10\%$, which are ascribed mainly to the finite grid resolution and partly to the finite extraction radius

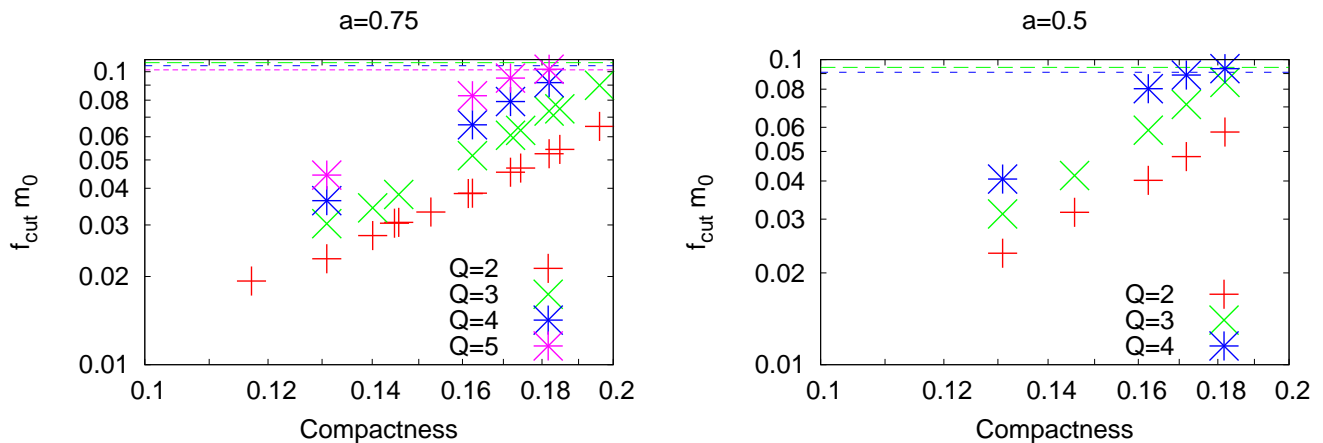


FIG. 24. The same as Fig. 23 but for $a = 0.75$ (left) and 0.5 (right). In both panels, $f_{\text{QNM}} > f_{\text{cut}}$ for $Q = 2$.

for Ψ_4 . Because ΔE and ΔJ depend on the choice of $\Omega_0 m_0$, we do not compare directly the results obtained for models with different values of $\Omega_0 m_0$ and accordingly models with different values of Q (see Table III).

Contributions from all the $l = 2-4$ modes of gravitational waves are taken into account. The $(l, |m|) = (2, 2)$ mode always contributes by $\gtrsim 85\%$ to ΔE and ΔJ . ΔE and ΔJ taken away by higher-mode gravitational waves are substantial for high mass-ratio binaries. For example, the $(3, 3)$ mode contributes by $\sim 2, 5, 7.5,$ and 10% for binaries with $Q = 2, 3, 4,$ and 5 , respectively. The $(4, 4)$ mode gravitational waves contribute by $1 \sim 2\%$ for binaries with $Q = 3-5$. These values depend only weakly on a and the EOS, and contributions of modes with $l \neq m$ are negligible compared to those of $l = m$ modes.

Table VI shows that $\Delta E/M_0$ and $\Delta J/J_0$ increase monotonically as the NS compactness, \mathcal{C} , increases for binaries with fixed values of (Q, a) . This is the same result as that obtained for nonspinning BH-NS binaries [31] and is explained by a longer inspiral phase for a softer EOS due to the later onset of mass shedding and the later tidal disruption. The ratio between these two values, $(\Delta J/J_0)/(\Delta E/M_0)$, decreases as \mathcal{C} increases. This agrees again with the result for the nonspinning BH cases and is explained by a relation $\Delta J/\Delta E \approx m/\Omega$ for a given angular harmonic of m and by the fact that more radiation is emitted from the orbit of a larger value of Ω for a softer EOS. Note that these arguments are based on little dependence of gravitational-wave luminosity in the inspiral phase on \mathcal{C} for a fixed value of a ; tidal correction to the luminosity in the inspiral phase is not important.

Table VI shows that $\Delta E/M_0$ does not depend strongly on a , while $\Delta J/J_0$ increases as a increases in many cases for a fixed value of \mathcal{C} . Remember that dE/df in the inspiral phase increases for a large value of a , as is given by Eq. (42). However, the orbital frequency, Ω , at the tidal disruption decreases for a large value of a due to the spin-orbit interaction. Because of these two competing effects, the binding energy at the tidal disruption depends only

weakly on a , and hence, $\Delta E/M_0$ does not change very much among different values of a . The increase of $\Delta J/J_0$ for a large value of a is due to the large value of dE/df in the inspiral phase, during which Ω is relatively low, and to the approximate relation $\Delta J \approx m\Delta E/\Omega$, which enhances the contribution of low-frequency gravitational waves.

Finally, we comment on the linear momentum ΔP radiated by gravitational waves and an associated kick velocity $v_{\text{kick}} \equiv \Delta P/M_0$ of the remnant BH. Because of the mass and spin asymmetries, the remnant BH achieves the kick velocity of $\sim 100-250$ km/s when the effect of tidal disruption is weak, e.g., for models HB-Q3M135a-5 and B-Q3M135. Although our results for ΔP do not converge as well as those for ΔE and ΔJ due to the slow convergence of $(l, m) \neq (2, 2)$ mode gravitational waves, the values of v_{kick} are in reasonable agreements with the fitting formula derived using the results of simulations for the binary BH merger [97, 98]. By contrast, v_{kick} is suppressed to $\lesssim 100$ km/s when tidal disruption occurs far outside the ISCO. The reason for this is that the tidal disruption suppresses significantly the gravitational radiation from the last inspiral and merger phases, during which the linear momentum is emitted most efficiently. This trend is consistent with the result found in our previous work [29].

V. SUMMARY

We performed numerical simulations for the merger of BH-NS binaries with various BH spins aligned or anti-aligned with the orbital angular momentum, using an AMR code SACRA with systematically chosen five piecewise polytropic EOSs. We investigated the dependence of the merger process, properties and structures of the remnant disk, properties of the remnant BH, gravitational waveforms, and their spectra on the spin of the BH and the EOS of the NS. In particular, we focused on the case

TABLE VI. Total radiated energy ΔE and angular momentum ΔJ carried away by gravitational waves. ΔE and ΔJ are normalized with respect to the initial ADM mass M_0 and angular momentum J_0 , respectively. We also show the ratio between ΔJ and ΔE .

Model	$\Delta E/M_0$ (%)	$\Delta J/J_0$ (%)	$(\Delta J/J_0)/(\Delta E/M_0)$
2H-Q2M135a75	0.58	16	27
1.5H-Q2M135a75	0.79	19	24
H-Q2M135a75	1.1	24	21
HB-Q2M135a75	1.4	26	19
B-Q2M135a75	1.7	29	17
2H-Q2M135a5	0.60	17	26
1.5H-Q2M135a5	0.79	19	24
H-Q2M135a5	1.2	24	20
HB-Q2M135a5	1.4	26	19
B-Q2M135a5	1.7	28	17
2H-Q2M135a-5	0.57	15	26
H-Q2M135a-5	1.1	19	16
HB-Q2M135a-5	1.4	19	14
B-Q2M135a-5	1.6	21	13
2H-Q2M12a75	0.40	12	30
H-Q2M12a75	0.79	19	24
HB-Q2M12a75	0.95	21	22
B-Q2M12a75	1.2	24	21
2H-Q2M145a75	0.73	19	25
H-Q2M145a75	1.5	27	19
HB-Q2M145a75	1.7	30	17
B-Q2M145a75	2.1	32	15
2H-Q3M135a75	0.72	20	28
1.5H-Q3M135a75	0.97	23	24
H-Q3M135a75	1.3	27	20
HB-Q3M135a75	1.6	30	19
B-Q3M135a75	2.0	34	17
2H-Q3M135a5	0.70	19	27
1.5H-Q3M135a5	0.94	22	23
H-Q3M135a5	1.4	26	19
HB-Q3M135a5	1.7	29	17
B-Q3M135a5	2.0	31	15
HB-Q3M135a-5	1.3	19	14
2H-Q3M145a75	0.88	22	25
H-Q3M145a75	1.7	31	18
HB-Q3M145a75	2.1	34	16
B-Q3M145a75	2.5	37	15
2H-Q4M135a75	0.81	23	28
H-Q4M135a75	1.5	31	21
HB-Q4M135a75	1.8	33	19
B-Q4M135a75	2.1	36	17
2H-Q4M135a5	0.72	19	27
H-Q4M135a5	1.5	27	19
HB-Q4M135a5	1.7	29	17
B-Q4M135a5	1.9	31	16
2H-Q5M135a75	0.83	24	29
H-Q5M135a75	1.6	33	20
HB-Q5M135a75	1.9	35	19
B-Q5M135a75	2.1	36	17

in which the BH has a prograde spin, and the tidal disruption of the NS by a companion BH plays an important role. We adopted a number of parameters for the mass ratio, NS mass, and BH spin. By preparing the initial condition with a distant orbit and a small eccentricity, we always tracked $\gtrsim 5$ quasicircular orbits in the inspiral phase and studied the merger phase in a realistic setting. The treatment of hydrodynamic equations and the estimation method of the disk mass are improved in this work. In the following, we summarize the conclusions in this paper:

1. It is shown that a prograde BH spin enhances the effect of NS tidal disruption by the spin-orbit interaction. The mass of the remnant disk increases as the BH spin increases because the ISCO radius of the BH becomes small. A remarkable point is that the BH-NS binary with a high mass ratio of even $Q = 5$ can form a sufficiently massive disk of $\gtrsim 0.1M_\odot$ for a wide range of the NS compactness if the BH has a prograde spin of $a = 0.75$. This amount of the disk mass for a high mass-ratio binary is hardly expected if the BH is nonspinning. This fact suggests that the formation of a BH-massive accretion disk system is a frequent outcome of the BH-NS binary merger with a prograde BH spin and may be encouraging for the merger scenario of a short-hard GRB. By contrast, the disk mass becomes very small if the BH has a retrograde spin.
2. It is shown that some portion of the disrupted material can extend to $\gtrsim 400$ km from the BH if the massive disk is formed. The maximum rest-mass density in the disk is larger for binaries with smaller values of Q because the ISCO radius is smaller for them. The extent of the disk could be large for a large value of Q . For such a remnant disk, the lifetime should be longer.
3. The spin parameter of the remnant BH depends primarily on the spin parameter of the initial BH, a , and the mass ratio, Q . In particular, extrapolation of our results suggests that the merger of an extremely spinning BH and an irrotational NS does not form an overspinning BH.
4. The gravitational waveform also depends strongly on the BH spin. The number of gravitational-wave cycles becomes larger for a prograde BH spin than that for a zero BH spin in the inspiral phase because an additional repulsive force due to the spin-orbit interaction reduces gravitational-wave luminosity and an approaching velocity of the binary. We found that the Taylor-T4 formula does not reproduce the phase evolution in the late inspiral phases accurately, especially when the mass ratio is large.
5. In our previous work for nonspinning BH-NS binaries, the waveforms are classified simply into two

categories: when tidal disruption of the NS occurs, the waveform is composed of an inspiral waveform and a prompt shutdown at the tidal disruption. When tidal disruption does not occur, the waveform is composed of inspiral and QNM waveforms. However, we find that the NS tidal disruption and the excitation of a QNM can occur simultaneously for binaries with a high mass ratio and a prograde BH spin. This is because the disrupted material cannot become axisymmetric before the prompt in-fall due to a larger BH areal radius for a larger value of Q . As a result, the material accretes onto the remnant BH coherently, and, therefore, the QNM of the remnant BH is excited, except for the case in which the extremely stiff EOS is adopted.

6. The cutoff frequency of the gravitational-wave spectrum is correlated with the NS compactness in a clear manner when the NS is disrupted, and the BH spin modifies this correlation. The prograde BH spin decreases the cutoff frequency for fixed values of \mathcal{C} and Q because the angular velocity at the tidal disruption becomes smaller than that for $a = 0$. The cutoff frequency is lower for a smaller value of \mathcal{C} for fixed values of Q and a , as in the case of nonspinning BH-NS binaries, because the tidal effect is stronger and the disruption occurs at a more distant orbit. The BH spin also modifies the spectrum for the inspiral phase. Specifically, the spectrum amplitude for a given frequency in the inspiral phase becomes large when the BH has a prograde spin, and this is consistent with the PN estimation. Both the low cutoff frequency and large spectrum amplitude in the inspiral phase for a prograde BH spin are encouraging for gravitational-wave astronomy to become a tool to investigate the NS compactness and EOS. It is noteworthy that the BH-NS binary with a high mass ratio of $Q \gtrsim 5$ is a more promising target for ground-based gravitational-wave detectors if the BH has a prograde spin and the NS tidal disruption occurs.

Finally, we list several issues to be explored in the future. Piecewise polytropic EOSs with two pieces employed in this paper are not accurate enough to model high-mass NSs with large central density of $\rho_{\max} \gtrsim 10^{15} \text{g/cm}^3$ [59]. More detailed (piecewise polytropic) EOSs are necessary to calculate gravitational waves from a BH-relatively massive NS binary merger for which the tidal deformation and disruption of the NS plays an important role, i.e., BH-NS binaries with moderately large BH spins of $a \gtrsim 0.75$. The implementation of detailed microphysics, such as a finite-temperature effect and a neutrino transport process, is essential even qualitatively to explore the evolution of the remnant BH-accretion disk system and to discuss the jet launch such that short-hard GRBs require. Recently, Sekiguchi developed a code to perform fully general relativistic simulation with the finite-temperature EOS and an approximate neu-

trino emission (the so-called leakage scheme) and succeed in simulating the stellar core collapse [99, 100] and the merger of binary NSs [101]. We plan to work on BH-NS binary mergers along these lines.

ACKNOWLEDGMENTS

K. K. is deeply grateful to Ericourgoulhon, Nicolas Vasset, and Benjamin D. Lackey for valuable discussion. We also thank Tetsuro Yamamoto for developing SACRA. Numerical computations of quasiequilibrium states were performed using the free library LORENE [33]. We thank members of the Meudon Relativity Group for developing LORENE. This work was supported by the Grant-in-Aid for Scientific Research (21340051), by the Grant-in-Aid for Scientific Research on Innovative Area (20105004), by the Grant-in-Aid for the Global COE Program “The Next Generation of Physics, Spun from Universality and Emergence,” by the HPCI strategic program of Japanese MEXT, by the Grant-in-Aid for Research Activity Start-up of JSPS (22840010), and by the Grant-in-Aid of JSPS.

Appendix: Convergence of gravitational waves and the remnant disk mass

This Appendix demonstrates that the convergence is approximately achieved for gravitational waves and masses of the remnant disks shown in Sec. IV. Figure 25 shows the evolution of the orbital angular velocity determined by Eq. (32) and gravitational waveforms obtained with different grid resolutions for models HB-Q4M135a75 and 2H-Q5M135a75. We perform an appropriate time shift in order to align the curves in the inspiral phase, and perform the rotation of $+$ and \times polarization modes of gravitational waveforms for $N = 42$ and 36. We note that the time to the merger, t_{merger} , is systematically longer for finer grid resolutions because numerical dissipation of the angular momentum is smaller [29, 31]. In both cases, the evolution of the orbital angular velocity, $\Omega(t)$, approximately agrees up to the merger, except for initial bursts associated with the junk radiation. The gravitational waveforms agree very well in the final ~ 4 orbits of the inspiral phase ($t \gtrsim 15$ ms), the merger phase, and the ringdown phase if the QNM is excited. By contrast, gravitational waveforms in the initial ~ 2 orbits depend strongly on the grid resolutions, because the early inspiral phase is strongly affected by the dissipation of the junk radiation. We conclude that the convergence is approximately achieved for gravitational waves in the late inspiral, merger, and ringdown phases.

Figure 26 shows the evolution of the rest mass located outside the AH, $M_{r>r_{\text{AH}}}$, with different grid resolutions for models HB-Q4M135a75 and 2H-Q5M135a75. This figure shows that the convergence is also approximately achieved for the mass of the remnant disk. Quantitatively, differences in $M_{r>r_{\text{AH}}}$ at ≈ 10 ms after the merger

are $\approx 2.9\%$ and $\approx 2.6\%$ for models HB-Q4M135a75 and 2H-Q5M135a75, respectively. If we assume the first-order

convergence for $M_{r>\tau_{\text{AH}}}$, the errors in the values obtained for $N = 50$ runs are $\approx 7.5\%$ and $\approx 6.8\%$ for models HB-Q4M135a75 and 2H-Q5M135a75, respectively.

-
- [1] B. P. Abbott et al., Rep. Prog. Phys. **72**, 076901 (2009).
- [2] T. Accadia et al., Class. Quantum Grav. **28**, 025005 (2011).
- [3] K. Kuroda and the LCGT Collaboration, Class. Quantum Grav. **27**, 084004 (2010).
- [4] L. Lindblom, Astrophys. J. **398**, 569 (1992).
- [5] M. Vallisneri, Phys. Rev. Lett. **84**, 3519 (2000).
- [6] J. S. Read, C. Markakis, M. Shibata, K. Uryū, J. D. E. Creighton, and J. L. Friedman, Phys. Rev. D **79**, 124033 (2009).
- [7] V. Ferrari, L. Gualtieri, and F. Pannarale, Phys. Rev. D **81**, 064026 (2010).
- [8] F. Pannarale, A. Tonita, and L. Rezzolla, Astrophys. J. **727**, 95 (2011).
- [9] F. Pannarale, L. Rezzolla, F. Ohme, and J. S. Read, arXiv:1103.3526.
- [10] P. Demorest, T. Pennucci, S. Ransom, M. Roberts, and J. Hessels, Nature **467**, 1081 (2010).
- [11] A. W. Steiner, J. M. Lattimer, and E. F. Brown, Astrophys. J. **722**, 33 (2010).
- [12] E. Nakar, Phys. Rep. **442**, 166 (2007).
- [13] W. H. Lee and E. Ramirez-Ruiz, New J. Phys **9**, 17 (2007).
- [14] R. D. Blandford and R. D. Znajek, Mon. Not. Roy. Astron. Soc. **179**, 433 (1977).
- [15] E. Berger et al., Nature **438**, 988 (2005).
- [16] W. Fong, E. Berger, R. Chornock, N. R. Tanvir, A. J. Levan, J. F. Graham, A. S. Fruchter, A. Cucchiara, and D. B. Fox, Astrophys. J. **730**, 26 (2011).
- [17] S. E. Woosley, Astrophys. J. **405**, 273 (1993).
- [18] P. Grandclément, Phys. Rev. D **74**, 124002 (2006); **75**, 129903(E) (2007).
- [19] K. Taniguchi, T. W. Baumgarte, J. A. Faber, and S. L. Shapiro, Phys. Rev. D **75**, 084005 (2007).
- [20] K. Taniguchi, T. W. Baumgarte, J. A. Faber, and S. L. Shapiro, Phys. Rev. D **77**, 044003 (2008).
- [21] F. Foucart, L. E. Kidder, H. P. Pfeiffer, and S. A. Teukolsky, Phys. Rev. D **77**, 124051 (2008).
- [22] K. Kyutoku, M. Shibata, and K. Taniguchi, Phys. Rev. D **79**, 124018 (2009).
- [23] M. Shibata and K. Uryū, Phys. Rev. D **74**, 121503(R) (2006).
- [24] M. Shibata and K. Uryū, Class. Quant. Grav. **24**, S125 (2007).
- [25] M. Shibata and K. Taniguchi, Phys. Rev. D **77**, 084015 (2008).
- [26] Z. B. Etienne, J. A. Faber, Y. T. Liu, S. L. Shapiro, K. Taniguchi, and T. W. Baumgarte, Phys. Rev. D **77**, 084002 (2008).
- [27] M. D. Duez, F. Foucart, L. E. Kidder, H. P. Pfeiffer, M. A. Scheel, and S. A. Teukolsky, Phys. Rev. D **78**, 104015 (2008).
- [28] Z. B. Etienne, Y. T. Liu, S. L. Shapiro, and T. W. Baumgarte, Phys. Rev. D **79**, 044024 (2009).
- [29] M. Shibata, K. Kyutoku, T. Yamamoto, and K. Taniguchi, Phys. Rev. D **79**, 044030 (2009).
- [30] M. D. Duez, F. Foucart, L. E. Kidder, C. D. Ott, and S. A. Teukolsky, Class. Quant. Grav. **27**, 114106 (2010).
- [31] K. Kyutoku, M. Shibata, and K. Taniguchi, Phys. Rev. D **82**, 044049 (2010).
- [32] S. Chawla, M. Anderson, M. Besselman, L. Lehner, S. L. Liebling, P. M. Motl, and D. Neilsen, Phys. Rev. Lett. **105**, 111101 (2010).
- [33] LORENE website, <http://www.lorene.obspm.fr/>.
- [34] G. B. Cook, Living Rev. Relativity **3**, 5 (2000).
- [35] L. Bildsten and C. Cutler, Astrophys. J. **400**, 175 (1992).
- [36] C. S. Kochanek, Astrophys. J. **398**, 234 (1992).
- [37] J. W. York, Phys. Rev. Lett. **82**, 1350 (1999).
- [38] H. P. Pfeiffer and J. W. York, Phys. Rev. D **67**, 044022 (2003).
- [39] S. Brandt and B. Brügmann, Phys. Rev. Lett. **78**, 3606 (1997).
- [40] M. Campanelli, C. O. Lousto, P. Marronetti, and Y. Zlochower, Phys. Rev. Lett. **96**, 111101 (2006).
- [41] J. G. Baker, J. Centrella, D.-I. Choi, M. Koppitz, and J. van Meter, Phys. Rev. Lett. **96**, 111102 (2006).
- [42] R. Beig, Phys. Lett. A **69**, 153 (1978).
- [43] A. Ashtekar and A. Magnon-Ashtekar, J. Math. Phys. **20**, 793 (1979).
- [44] J. M. Bowen and J. W. York, Phys. Rev. D **21**, 2047 (1980).
- [45] A. Ashtekar and B. Krishnan, Living Rev. Relativity **7**, 10 (2004).
- [46] E.ourgoulhon and J. L. Jaramillo, Phys. Rep. **423**, 159 (2006).
- [47] L.-M. Lin and J. Novak, Class. Quant. Grav. **24**, 2665 (2007).
- [48] G. B. Cook and B. F. Whiting, Phys. Rev. D **76**, 041501 (2007).
- [49] G. Lovelace, R. Owen, H. P. Pfeiffer, and T. Chu, Phys. Rev. D **78**, 084017 (2008).
- [50] S. Dain, C. O. Lousto, and Y. Zlochower, Phys. Rev. D **78**, 024039 (2008).
- [51] S. Bonazzola, E.ourgoulhon, and J.-A. Marck, Phys. Rev. D **56**, 7740 (1997).
- [52] H. Asada, Phys. Rev. D **57**, 7292 (1998).
- [53] M. Shibata, Phys. Rev. D **58**, 024012 (1998).
- [54] S. A. Teukolsky, Astrophys. J. **504**, 442 (1998).
- [55] G. Faye, L. Blanchet, and A. Buonanno, Phys. Rev. D **74**, 104033 (2006).
- [56] L. Blanchet, A. Buonanno, and G. Faye, Phys. Rev. D **74**, 104034 (2006).
- [57] L. Blanchet, Phys. Rev. D **65**, 124009 (2002).
- [58] J. M. Lattimer and M. Prakash, Science **304**, 536 (2004).
- [59] J. S. Read, B. D. Lackey, B. J. Owen, and J. L. Friedman, Phys. Rev. D **79**, 124032 (2009).
- [60] I. H. Stairs, Science **304**, 547 (2004).
- [61] J. M. Lattimer and M. Prakash, Astrophys. J. **550**, 426 (2001).
- [62] In this paper, we determine the stiffness simply as the

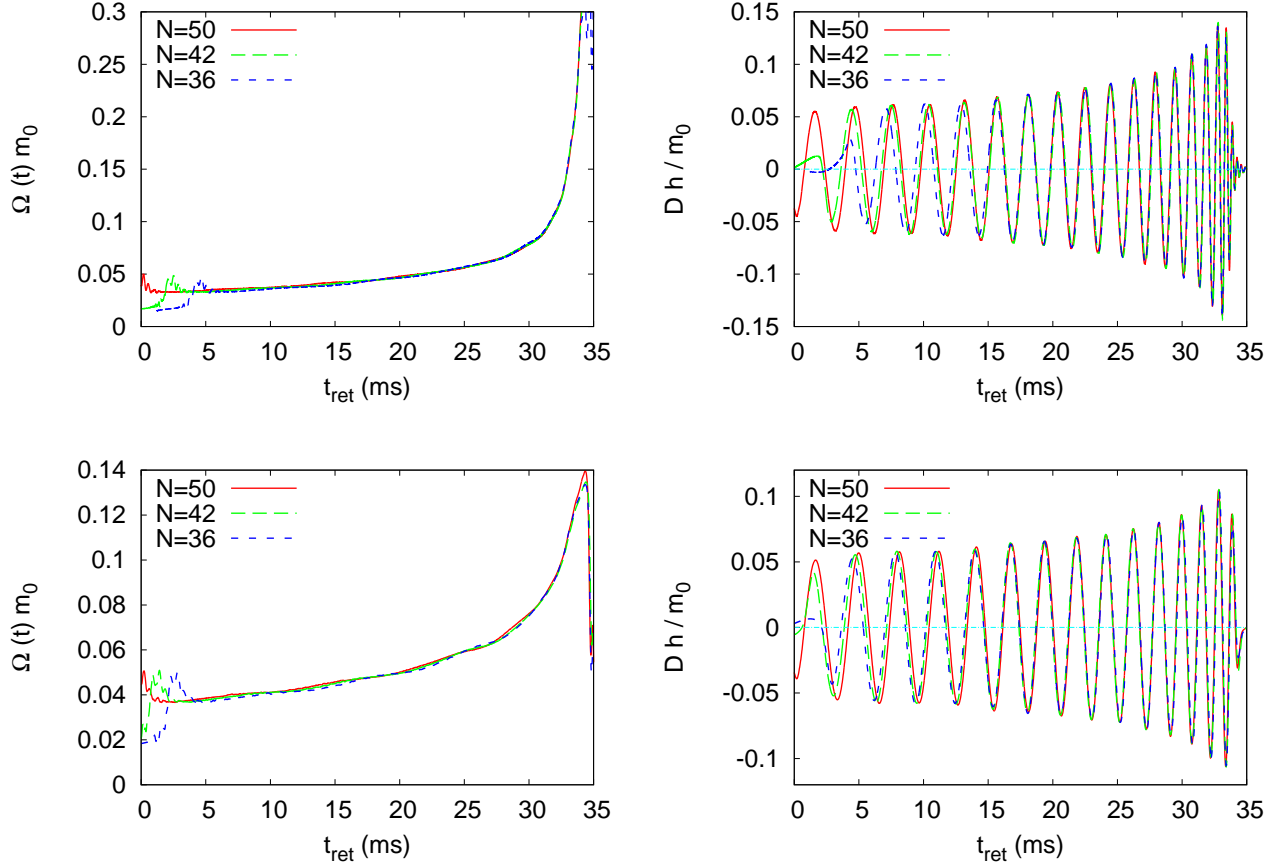


FIG. 25. Comparisons of evolution of the orbital angular velocity and gravitational waveforms for models HB-Q4M135a75 (top) and 2H-Q5M135a75 (bottom) with appropriate time shifts.

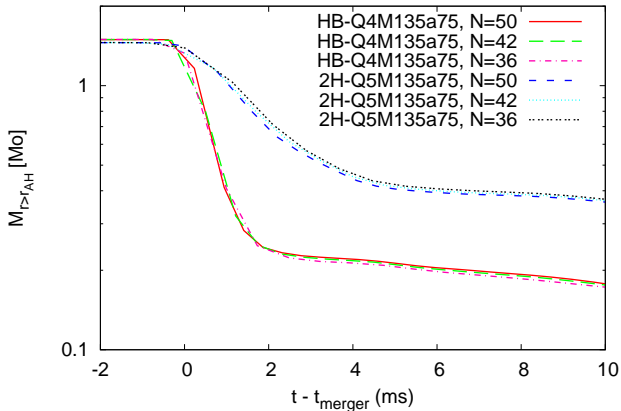


FIG. 26. Comparisons of evolution of the remnant disk masses for models HB-Q4M135a75 and 2H-Q5M135a75.

magnitude of the pressure for the nuclear-density region.

- [63] B. D. Lackey, K. Kyutoku, M. Shibata, P. R. Brady, and J. L. Friedman, to be published.
 [64] M. Shibata, Prog. Theor. Phys. **96**, 917 (1996).

- [65] P. Wiggins and D. Lai, Astrophys. J. **532**, 530 (2000).
 [66] In this paper, “the ISCO radius” always represents “the ISCO radius in the Boyer-Lindquist coordinates,” which is physical in the sense that it gives the proper circumferential length for the equatorial circular orbit. It should be noted that the coordinate radius of the ISCO in our simulation is different from the Boyer-Lindquist one.
 [67] J. M. Bardeen, W. H. Press, and S. A. Teukolsky, Astrophys. J. **178**, 347 (1972).
 [68] L. Blanchet, Living Rev. Relativity **9**, 4 (2006).
 [69] T. Yamamoto, M. Shibata, and K. Taniguchi, Phys. Rev. D **78**, 064054 (2008).
 [70] M. Shibata and T. Nakamura, Phys. Rev. D **52**, 5428 (1995).
 [71] T. W. Baumgarte and S. L. Shapiro, Phys. Rev. D **59**, 024007 (1998).
 [72] B. Brüggmann, J. A. González, M. Hannam, S. Husa, U. Sperhake, and W. Tichy, Phys. Rev. D **77**, 024027 (2008).
 [73] A. Kurganov and E. Tadmor, J. Comput. Phys. **160**, 241 (2000).
 [74] C. Reisswig and D. Pollney, arXiv:1006.1632.
 [75] M. Boyle, D. A. Brown, L. E. Kidder, A. H. Mroué, H. P. Pfeiffer, M. A. Scheel, G. B. Cook, and S. A. Teukolsky, Phys. Rev. D **76**, 124038 (2007).

- [76] L. Santamaria, F. Ohme, P. Ajith, B. Brügmann, N. Dorband, M. Hannam, S. Husa, P. Mösta, D. Pollney, C. Reisswig, E. L. Robinson, J. Seiler, and B. Krishnan, *Phys. Rev. D* **82**, 064016 (2010).
- [77] L. E. Kidder, *Phys. Rev. D* **77**, 044016 (2008).
- [78] T. Damour and A. Nagar, arXiv:0906.1769.
- [79] L. E. Kidder, *Phys. Rev. D* **52**, 821 (1995).
- [80] L. G. Fishbone, *Astrophys. J.* **185**, 43 (1973).
- [81] J.-A. Marck, *Proc. Roy. Soc. London* **385**, 431 (1983).
- [82] M. Ishii, M. Shibata, and Y. Mino, *Phys. Rev. D* **71**, 044017 (2005).
- [83] J. E. McClintock and R. A. Remillard, in *Compact Stellar X-ray Sources*, edited by W. H. G. Lewin and M. van der Klis (Cambridge University Press, 2006).
- [84] K. Belczynski, T. Bulik, C. L. Fryer, A. Ruiter, F. Valsecchi, J. S. Vink, and J. R. Hurley, *Astrophys. J.* **714**, 1217 (2010).
- [85] F. Foucart, M. D. Duez, L. E. Kidder, and S. A. Teukolsky, *Phys. Rev. D* **83**, 024005 (2011).
- [86] R. Penrose, in *general relativity: an Einstein centenary survey*, edited by S. W. Hawking and W. Israel (1979).
- [87] E. Berti, V. Cardoso, and A. O. Starinets, *Class. Quantum Grav.* **26**, 163001 (2009).
- [88] K. Uryū, F. Limousin, J. L. Friedman, E. Gourgoulhon, and M. Shibata, *Phys. Rev. Lett.* **97**, 171101 (2006).
- [89] K. Uryū, F. Limousin, J. L. Friedman, E. Gourgoulhon, and M. Shibata, *Phys. Rev. D* **80**, 124004 (2009).
- [90] M. Saijo and T. Nakamura, *Phys. Rev. Lett.* **85**, 2665 (2000).
- [91] M. Saijo and T. Nakamura, *Phys. Rev. D* **63**, 064004 (2001).
- [92] M. Punturo et al., *Class. Quantum Grav.* **27**, 194002 (2010).
- [93] L. Baiotti, T. Damour, B. Giacomazzo, A. Nagar, and L. Rezzolla, *Phys. Rev. Lett.* **105**, 261101 (2010).
- [94] L. Baiotti, T. Damour, B. Giacomazzo, A. Nagar, and L. Rezzolla, *Phys. Rev. D* **84**, 024017 (2011).
- [95] We refer to f_{dam} as f_{cut} throughout in the previous work [31]. In the present paper, we distinguish f_{dam} from f_{cut} because the method for determining f_{dam} is different from that for f_{cut} .
- [96] The relation between $f_{\text{cut}}m_0$ and \mathcal{C} is different from the one obtained in Ref. [31] due to the different definition of f_{cut} .
- [97] L. Rezzolla, *Class. Quantum Grav.* **26**, 094023 (2009).
- [98] Y. Zlochower, M. Campanelli, and C. O. Lousto, *Class. Quantum Grav.* **28**, 114015 (2011).
- [99] Y. Sekiguchi, *Prog. Theor. Phys.* **124**, 331 (2010).
- [100] Y. Sekiguchi and M. Shibata, *Astrophys. J.* **737**, 6 (2011).
- [101] Y. Sekiguchi, K. Kiuchi, K. Kyutoku, and M. Shibata, *Phys. Rev. Lett.* **107**, 051102 (2011).